

# Influence of environmental nutrient conditions on *Gymnodinium breve* (Dinophyceae) population dynamics: a numerical study

Gang Liu, Gerald S. Janowitz\*, Daniel Kamykowski

Department of Marine, Earth & Atmospheric Sciences, North Carolina State University, Raleigh, North Carolina 27695-8208, USA

**ABSTRACT:** A model of *Gymnodinium breve* population dynamics modified from Liu et al. (2001; Mar Ecol Prog Ser 210:101–124) is used to investigate the influence of various nutrient conditions on the population increase of an alongshore population filament of *G. breve* cells as it moves onshore across a continental shelf. The environmental conditions in the model are derived from measurements or theory applicable to bloom development on the west Florida shelf. The simulations indicate that the potential nutrient input patterns here represented by nitrogen sources on the shelf, i.e., offshore, mid-shelf and coastal upwellings, a *Trichodesmium*-released surface nitrogen source associated with multi-nutrient ocean fertilization by air-borne dust input, and a coastal surface plume are all eligible to trigger and/or support a *G. breve* bloom. However, the occurrence, timing, location, duration, and intensity of the bloom are determined by nitrogen concentration, input location, and temporal availability. Some nitrogen support at the offshore initiation stage of population growth may induce earlier bloom development, but without additional nitrogen input in coastal regions, the bloom may not fully develop. As long as the nitrogen is available continuously from offshore through coastal regions, a *G. breve* population can develop into a fish-killing intensity ( $1$  to  $2.5 \times 10^5$  cells  $l^{-1}$ ) in a month or so from a background concentration of  $<1000$  cells  $l^{-1}$  with a maximum growth rate of  $\sim 0.16$  doublings  $d^{-1}$ . An explosive growth stage is not present for the total population in the simulations in which fish-killing cell concentrations are developed in 30 d. However the illusion of explosive growth may be created by the first appearance of a high *G. breve* population density at the surface late in bloom development. In some cases, daily averaged surface concentration can increase by a factor of 10 in 2 d and increase from a background level of 500 cells  $l^{-1}$  to bloom levels of  $10^4$  cells  $l^{-1}$  in 8 d due primarily to surface accumulation resulting from appropriately directed swimming behavior. This numerical investigation further demonstrates that the vertical migration of *G. breve* can play a critical role not only in the efficient utilization of natural resources, but also in the population distribution.

**KEY WORDS:** Model · Dinoflagellate · *Gymnodinium breve* · Population dynamics · Behavior · Nutrients

Resale or republication not permitted without written consent of the publisher

## INTRODUCTION

A toxic red tide (also called harmful algal bloom [HAB]) dinoflagellate, *Gymnodinium breve* has a US distribution from the Gulf of Mexico to the South Atlantic Bight (Tester & Steidinger 1997). This microalga

produces neurotoxins and hemolytic substances that have caused massive mortalities of marine animals, human neurotoxic shellfish poisoning, human respiratory irritation (Rounsefell & Nelson 1966), and alteration of marine habitats and trophic structure in the Gulf of Mexico almost every year in recent decades (Steidinger & Vargo 1988, Tester et al. 1991).

HABs have been divided into a sequence of 4 distinct stages: initiation, growth, maintenance, and decline

\*Corresponding author. E-mail: janowitz@ncsu.edu

(Steidinger & Baden 1984). Physical factors (e.g., aggregation, dissipation, advection, and mixing), biological factors (e.g., organism's behavior, physiological state, life cycle, and tolerance for environmental conditions such as nutrients, light, temperature, salinity), and chemical factors (e.g., nutrient support) all interact to determine not only the timing and location of the ultimate biomass achieved and the termination mode of the blooms but also the impacts on the environment. Among numerous external factors which may contribute to the initiation, growth and maintenance of *Gymnodinium breve* blooms, the nutrient supply is considered one of the most important factors and is emphasized in this article. The autotrophic diel vertical migration of *G. breve* is hypothesized to have significant and fundamental effects on its population dynamics, and consequently on its red tide dynamics through the active pursuit of environmental resources, particularly nutrient resources, resulting in active population redistribution (Seliger et al. 1970, 1971, Tyler & Seliger 1978, Dahl & Tangen 1993, Kamykowski & Yamazaki 1997).

Numerous investigations have been conducted on *Gymnodinium breve* and many hypotheses have been proposed to explain the characteristics, behaviors, and population dynamics of its blooms (Tester & Steidinger 1997, Steidinger et al. 1998). However, our knowledge of *G. breve*, its response to environmental cues, and its population dynamics are still inadequate to understand the complex and integrated mechanisms that contribute to its blooms. Under these circumstances, the study of *G. breve* population dynamics by means of numerical simulation which incorporates current knowledge provides an important and powerful approach to formulate and test hypotheses and to guide future investigation and experiment. A recently developed individual-based, Eulerian type *G. breve* population dynamics model (Liu, Janowitz, and Kamykowski 2000, hereinafter referred to as LJK) focusing on the influence of diel vertical migration of *G. breve* on its population dynamics successfully simulated the observations in a laboratory experiment under uniform nutrient replete conditions (Kamykowski et al. 1998). The LJK model is an application of the Expanded Eulerian Approach described in Janowitz & Kamykowski (1999).

A 1-dimensional *Gymnodinium breve* population dynamics model, considering the variation in external nutrient condition in 2-dimensional settings, is herein developed based on LJK. The influence of temporally and spatially varying external nutrient condition, here represented by nitrogen, on selected aspects of the field population dynamics of *G. breve* is simulated to investigate some important hypotheses on the relationships between nutrient supply and cell behavior on the

development of *G. breve* red tides on the west Florida shelf.

This paper is organized in the following order. The related background knowledge and hypotheses on development of *Gymnodinium breve* red tides on the west Florida shelf are introduced first, followed by the structure of the model. Then, several different environmental nutrient scenarios related to the background hypotheses are constructed for numerical simulation. Finally, simulation results and comparisons are presented and tests of the hypotheses are discussed.

## Background

*Gymnodinium breve* is common in the Gulf of Mexico all year long at background cell concentrations of  $\sim 1000$  cells  $l^{-1}$  (Geesey & Tester 1993). The harmful impacts caused by *G. breve* only occur when cell concentrations increase significantly above the low background concentrations. *G. breve* blooms are usually seasonal in late summer-early fall, but can occur any time of the year on the west Florida shelf (Tester & Steidinger 1997, Steidinger et al. 1998). They generally are located between Tampa Bay and Charlotte Harbor, Florida (Tester & Steidinger 1997, Steidinger et al. 1998).

*Gymnodinium breve* blooms usually start offshore in typically oligotrophic waters between 18 and 74 km offshore central Florida at depths of 12 to 40 m (Steidinger 1973, 1975, Steidinger & Haddad 1981) and can take about a month or so to develop into a fish-killing bloom ( $1$  to  $2.5 \times 10^5$  cells  $l^{-1}$ ) depending on environmental conditions (e.g., Tester & Steidinger 1997, Steidinger et al. 1998). *G. breve* red tides usually are monospecific and lack grazers (Steidinger 1973).

The west Florida shelf is a complex area of mixing between the Caribbean-derived anticyclonic Loop Current, the West Florida Estuarine Waters, and the Florida Bay Waters (Chew 1955, Austin & Jones 1974). The Loop Current is a major force driving circulation on the west Florida shelf through the formation of detached eddies or by direct contact with the shelf. The initiation of *Gymnodinium breve* red tides has been associated with the fronts caused by intrusions of the Loop Current (its onshore-offshore meanders) or its cyclonic eddies. At times these penetrate along the bottom into depths of 30 m or less on the outer continental shelf and are thus within the 18 to 74 km suggested initiation zone (e.g., Maul 1975, Steidinger & Haddad 1981, Tester & Steidinger 1997, Steidinger et al. 1998). The bloom development may also be associated with the intrusion of upwelled oceanic Loop Current waters into coastal region (e.g., Haddad & Carder 1979). The mid-shelf front maintained by seasonal wind reversals along the Florida west coast may serve

as a growth and accumulation region for *G. breve* blooms and contribute to the re-inoculation of near-shore waters (e.g., Tester & Steidinger 1997). The coastal surface nutrient plumes associated with freshwater outflow may support the growth and maintenance stages of the red tides (e.g., Chew 1956). The upwellings and surface plume are hypothesized to be key nutrient supply mechanisms for *G. breve* blooms on the west Florida shelf (Penta 2000). Further, Penta (2000) suggested that iron (and possibly other nutrients; Duce 1986) in the air-borne dust coming from Africa may be an important nutrient resource for the initiation and development of *G. breve* red tides. This iron-containing dust may fertilize the surface water on the west Florida shelf for the growth of *Trichodesmium* sp., a phytoplanktonic nitrogen-fixer capable of excreting organic nitrogen derived from nitrogen gas. An estimated 50% of the nitrogen fixed by *Trichodesmium* leaks into the surrounding water and may act as a possible trigger of *G. breve* blooms. The nutrient condition on the west Florida shelf typically is oligotrophic. However, an intermediate red tide level of  $1 \times 10^6$  cells  $l^{-1}$  requires initial nutrient stocks of  $8.0 \mu M$   $NO_3 l^{-1}$  (Wilson 1966, Vargo & Howard-Shamblott 1990) to sustain this population level. Although this concentration of inorganic nitrogen is usually not found within 2 to 4 km off the Florida coast (usually less than  $0.2 \mu M$   $l^{-1}$ ; Dragovich & May 1961, Dragovich et al. 1963, Vargo & Shanley 1985), the nitrogen concentration has been as high as 3 to 6  $\mu M$  for nitrate and 6 to 7  $\mu M$  for ammonium ion in the bloom regions.

*Gymnodinium breve* blooms can be transported onshore depending on hydrological and meteorological conditions, largely influenced by wind and wind-induced upwelling or downwelling (e.g., Tester & Steidinger 1997). The west Florida shelf is regularly subjected to periods of upwelling and downwelling as a result of the orientation of the Florida peninsula in relation to the passage of synoptic scale weather systems (Mitchum & Sturges 1982, Marmorino 1983a,b). Under an appropriate hydrographic setting, the onshore and offshore transports associated with these coastal upwelling and downwelling events can associate seed populations with the required nutrients to initiate and support *G. breve* blooms.

### Model description

In the present model, we consider a 2-dimensional filament of *Gymnodinium breve* cells oriented in the along-shore direction. The cell concentration and all external conditions are independent of the alongshore coordinate  $y$ . We also assume a constant water depth over the entire shelf. The filament is taken to move

onshore from an offshore location to a coastal region with a vertically uniform onshore velocity in the absence of lateral and vertical mixing. We consider an onshore-vertical cross-section of this filament and move along with this cross-section with the onshore velocity. In the assumed absence of mixing with adjacent cross-sections, cells in the cross-section remain in the cross-section, and the nutrient field experienced by the cross-section varies only with time and the vertical coordinate. A 1-dimensional (vertical position), time-dependent model which includes 4 variables to describe internal cellular states is all that is required to describe changes in this cross-section. Our 1-dimensional model is constructed to test the influence of different specified nutrient supply scenarios on the initiation, growth and maintenance of *G. breve* blooms.

The present *Gymnodinium breve* population dynamics model is developed from the LJK model. The model is of the Expanded Eulerian type (Janowitz & Kamykowski 1999). The purpose of LJK was to simulate the observations in a laboratory experiment with *G. breve* under a nutrient replete condition (Kamykowski et al. 1998). Some modifications are made to LJK so that this new model is applicable to deeper water columns, to wider irradiation ranges especially in very-low-light regimes, and in the presence of nutrient gradients, which were not present in LJK. Since the modifications are only present in the ranges not experienced by the cells in the LJK simulations, this present model is a version of LJK applicable to more complicated situations while not changing the simulation results for the experiment simulated in LJK. Except for its photosynthesis and diel vertical migration submodels, our new population dynamics model is exactly the same as LJK, including the internal states considered and their ranges. In this modified model, we use values of the parameters from LJK which were determined under observed nutrient replete conditions. All the equations in the present model are listed in Appendix 1, while only the modifications are given in detail below. See LJK for the details of the rest of the model, including the methods used to determine parameters. All the variables and parameters and their specified values for the present model are summarized in Table A1 of Appendix 1.

The governing equation for the number of identical cells per unit volume,  $\underline{C}$ , in  $z, Cn, N, H_c, E_3$  space is:

$$\frac{\partial \underline{C}}{\partial t} + \frac{\partial (V_z \underline{C})}{\partial z} + \frac{\partial (V_{Cn} \underline{C})}{\partial Cn} + \frac{\partial (V_N \underline{C})}{\partial N} + \frac{\partial (V_{H_c} \underline{C})}{\partial H_c} + \frac{\partial (V_{E_3} \underline{C})}{\partial E_3} = \text{Gains(reproduction)} \quad (1)$$

Here,  $Cn, N, H_c,$  and  $E_3$  are the internal cellular states used as independent variables in the model in addition to depth ( $z$ ) and time ( $t$ ), as in LJK. These additional independent variables are the internal cellular carbon

(excluding the internal carbon in protein), internal cellular nitrogen, the extent of cumulative photoinhibition, and the cellular sun-shade acclimation state represented by 3 d light exposure in the model, respectively.  $V_z$  is swimming velocity of the cells. The generalized advective velocities,  $V_{Cn}$ ,  $V_N$ ,  $V_{H_c}$ , and  $V_{E_3}$ , are the change rates of the respective internal states as experienced by the cells and are functions of the internal cellular states, the external photosynthetically active radiation (PAR) and nutrient fields. All of the submodels used to determine these velocities are given in Appendix 1, and the detailed explanation of the unmodified submodels is given in LJK. In the model,  $z$  is positive upwards with  $z = 0$  at the surface. The gain term on the right hand side is the rate of increase or decrease in cell number due to reproduction. Parent cells are lost and daughter cells gained as cells divide. Since bloom formation is the object of the present model, no loss terms due to grazing, mortality, or other losses are included. As a further simplification, no changes in the external nutrient fields due to uptake are considered under the assumption that a *Gymnodinium breve* population that is blooming is not limited by nutrients. Though these model attributes may be considered unrealistic in a natural context, they do allow the model to focus on cell behavior as associated with bloom initiation, growth and maintenance. The approach used here can be expanded to include bloom dissipation and a broader involvement of *G. breve* with other organisms as needed. Moving with the cross-section,  $\underline{C}$  is independent of  $x$  and  $y$ .

The upwind finite differencing scheme is applied to construct the model. Each independent field is discretized into a finite number of intervals between its minimum and maximum value. We now discuss the changes in the model from that in LJK.

### Photosynthesis submodel

In LJK, with constant surface illumination, PAR exceeded  $8 \mu\text{mol quanta m}^{-2} \text{s}^{-1}$  for the whole water column (1.6 m depth) during the light hours. This PAR intensity was low but still greater than the *Gymnodinium breve* compensation light intensity,  $I_c$ , which is  $6 \mu\text{mol quanta m}^{-2} \text{s}^{-1}$  (Shanley & Vargo 1993). The light intensity,  $I$ , may be very weak at depth in a deep water column and everywhere in the water column early and late in the day. Thus, a photosynthesis equation applicable to very low light regimes is required. The net photosynthetic rate is now taken as negative when  $I < I_c$  and approaches the respiration rate,  $-R_m$ , when the light intensity goes to 0. The potential photosynthetic rate of cells adapted to light intensity lower than the compensation intensity is assumed now to be

suppressed compared with cells which are adapted to light intensity higher than the compensation intensity. For these reasons, the photosynthesis submodel used in LJK is modified for very-low-light conditions, and the new set of the net photosynthesis equations for *G. breve* is as follows. In the following equations  $E_3$ ,  $I$ ,  $I_k$ , and  $I_c$  have been scaled by  $1.0 \mu\text{mol quanta m}^{-2} \text{s}^{-1}$  and are dimensionless in the respective equations. When  $I \geq I_c$ , the photosynthetic rate is:

$$\frac{dCn_{photo}}{dt} = Q \cdot \tanh(E_3) \cdot \left\{ 1.0 - \exp\left(-\frac{I}{I_k} [\tanh(I - I_c)]\right) \right\} \quad (2)$$

where  $I_k$  is the saturation light intensity and defined in LJK. During the daylight period, when  $I_c > I \geq 0$ ,

$$\frac{dCn_{photo}}{dt} = R_m \cdot \left\{ -1 + \frac{I}{A} + \left(1 - \frac{I_c}{A}\right) \cdot \exp\left[\frac{A+1}{I_c} (I - I_c)\right] \right\} \quad (3)$$

and

$$Q = [P_{md} + H_c(P_l - P_{md})] \quad (4)$$

$$A = \frac{Q \cdot \tanh(E_3)}{R_m E_3} I_c^2 + I_c - 1 \quad (5)$$

where,  $P_{md}$  and  $P_l$  are discussed in detail in LJK. See Table A1 for the notations and the values of the parameters. Eq. (3) for  $I < I_c$  is obtained by requiring that the net photosynthetic rate, which is equal to 0 at  $I = I_c$ , be equal to the respiration rate,  $-R_m$ , at  $I = 0$ , and that at  $I = I_c$ , the slope of the P-I curve of (2) equal to the slope of the P-I curve of (3). We utilized dark respiration rate of the *G. breve*,  $R_m$ , of  $0.333 \text{ pmol C cell}^{-1} \text{ h}^{-1}$  and its compensation light threshold,  $I_c$ , of  $6 \mu\text{mol quanta m}^{-2} \text{s}^{-1}$  (Shanley & Vargo 1993). However, the same method can be used to determine the constants for other values of  $R_m$  and  $I_c$ . Note that this set of equations gives different results only for the cells experiencing the light intensity lower than the light intensity experienced by the cells in the LJK simulations. So this modification leaves those results intact. A demonstration of the P-I curves given by this set of equations is shown in Fig. 1, for the scaled, dimensionless  $E_3$  of 1, 50, 100, and  $500 \mu\text{mol quanta m}^{-2} \text{s}^{-1}$ , respectively. These curves are obtained at noon, assuming no photoinhibition. The relationship among the curves when  $I < I_c$  may be thought to represent increased respiration in dark-adapted cells burdened with more photosynthetic machinery.

The governing equation for the internal cellular carbon in LJK is rearranged for this model. The equation for the daylight period is:

$$V_{Cn} = \frac{dCn}{dt} = \frac{dCn_{photo}}{dt} - \frac{dCn_{protein}}{dt} \quad (6)$$

and for the dark period:

$$V_{Cn} = \frac{dCn}{dt} = -R_m - \frac{dCn_{protein}}{dt} \quad (7)$$

where the second term on the right hand sides of Eqs. (6) & (7) is the loss of carbon to protein synthesis; see LJK for the details of that equation.

### Diel vertical migration submodel

The present diel vertical migration submodel is adapted from the LJK migration submodel with the only modifications related to the external nutrient condition. As in LJK, nitrate is the only nitrogen form considered and acts as a proxy for all nitrogen sources, while nitrogen in turn acts as a proxy for all nutrient sources. In both models, the migratory behavior of *Gymnodinium breve* is hypothesized to be influenced by internal cellular biochemical and physiological states, external environmental conditions, and endogenous circadian rhythms. The characteristics of the hypothesized internal and external influences vary with time during the diel cycle and modulate the strength of the endogenous circadian rhythm. The swimming behavior control is different for the light and dark period. The dark-controlling period is further split into 3 sub-periods: before midnight, after midnight but more than 2 h from sunrise, and the 2 h period prior to sunrise.

In LJK, the nitrate field was vertically uniform at 150  $\mu\text{M}$   $\text{NO}_3\text{-N}$ , a replete condition. The vertical

migration submodel in LJK did not have a mechanism to adjust the swimming orientation and speed if the ambient nitrate concentration experienced by cells varied with depth. If 1 principal purpose of vertical migratory behavior is to utilize the environmental resources efficiently, a cell exposed to a low ambient nitrate concentration may be capable of seeking a depth with higher nitrate concentration by detecting the direction of increasing nitrate (Willey & Waterbury 1989, Ikegami et al. 1995, Lee et al. 1999). The nitrate gradient must be large enough to be detected by the cell. In this modified model, an external nitrate gradient threshold ( $\text{GRAD}[\text{NO}_3]_{\text{ori}}$ ) of 0.01  $\mu\text{M m}^{-1}$  is set as the minimum gradient that *Gymnodinium breve* can sense. If the ambient nitrate gradient is less than this threshold, *G. breve* assumes higher nitrate concentration at depth. Except for the modifications presented below, all the rules in the vertical migration submodel are adopted from LJK. All the rules used for swimming orientation control in our new model and the associated swimming speed are summarized in Table A2 of Appendix 1.

For the cells which are not forced to descend by photoinhibition during the light period, there are 2 major internal carbon thresholds for swimming orientation control as in LJK: the higher threshold,  $C_{N_{\text{Full}}}$ , at 87.3  $\text{pmol C cell}^{-1}$  and the lower threshold,  $C_{N_{\text{High}}}$ , at 68.4  $\text{pmol C cell}^{-1}$ . The swimming priority of a cell whose internal carbon concentration is equal to or greater than  $C_{N_{\text{Full}}}$  changes from photosynthesis to nitrate uptake. Its swimming orientation, in our new model, is determined by both its ambient nitrate concentration and the ambient vertical gradient of nitrate concentration. An ambient nitrate concentration threshold,  $[\text{NO}_3]_{\text{th}}$ , of 1.26  $\mu\text{M}$   $\text{NO}_3\text{-N}$ , which was introduced in LJK, is the first criterion used to determine the swimming orientation for the cell. At this nitrate concentration, the nitrate uptake rate of a cell is 75% of its potential maximum uptake rate, i.e.:

$$\frac{[\text{NO}_3]_{\text{th}}}{K_N[\text{NO}_3]_{\text{th}}} = 0.75 \quad \text{or} \quad [\text{NO}_3]_{\text{th}} = 3.0K_N = 1.26 \mu\text{M NO}_3 \quad (8)$$

with the half-saturation constant,  $K_N$ , of 0.42  $\mu\text{M N}$  (Steidinger et al. 1998). If the ambient nitrate concentration is greater than the threshold, the cell descends until it reaches a depth where the ambient nitrate concentration drops to the threshold; and then, the cell rests at this depth. If the ambient nitrate concentration is lower than the threshold, the ambient vertical gradient of nitrate concentration is examined; if the gradient is negative or less than the minimum positive gradient threshold of 0.01  $\mu\text{M m}^{-1}$ , the cell descends until its ambient nitrate concentration reaches the threshold ( $[\text{NO}_3]_{\text{th}}$ ), and then the cell rests there. If the nitrate

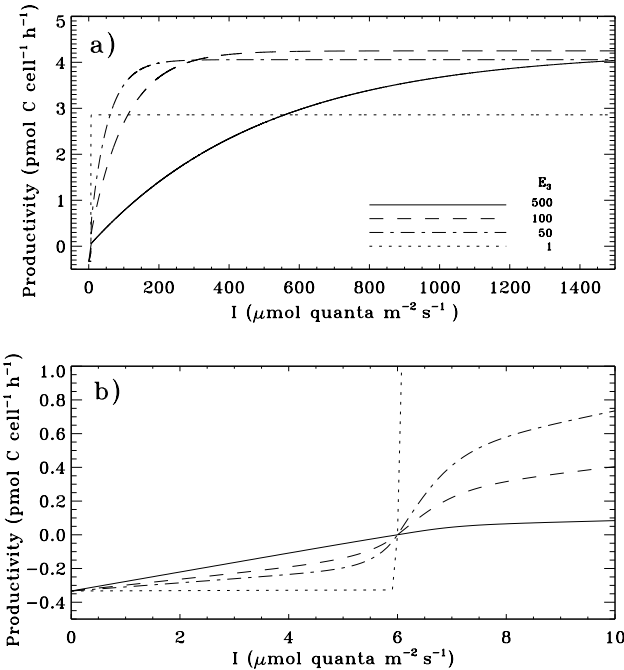


Fig. 1. P-I curves given by photosynthesis Eqs. (2) & (3) for cells with 3 d PAR exposures of 1, 50, 100, and 500  $\mu\text{mol quanta m}^{-2} \text{s}^{-1}$ , respectively, over (a) a PAR intensity range of [0, 1500] and (b) its subrange [0, 10] at the low-light end

gradient is positive and greater than  $0.01 \mu\text{M m}^{-1}$ , the cell ascends until its ambient nitrate concentration reaches the threshold ( $[\text{NO}_3]_{th}$ ), and then the cell rests there. For cells in this category (i.e.,  $Cn \geq Cn_{Full}$ ), the swimming speed for ascent, not present in LJK, is:

$$V_z = S_{accli} \left\{ 0.2 + 0.8 \left( 1 - \frac{[\text{NO}_3(z)]}{K_N + [\text{NO}_3(z)]} \right) \right\} \left\{ \frac{Cn_{max} - Cn}{Cn_{max} - Cn_{High}} \right\}^{\frac{1}{2}} \quad (9)$$

The swimming speed for descent remains the same as in LJK (see Eq. [A27]). These swimming speeds are acclimated to both internal cellular carbon concentration and ambient nitrate concentration. Note the difference in the internal carbon-related factors among the 3 equations (Eqs. [9] or [A26] & [A27]). The higher the internal carbon concentration, the faster the speed for the descending cells, but the slower the speed for the ascending cells; the higher the ambient nitrate concentration, the slower the speed. Cells which have more internal carbon descend faster or ascend slower because they have less demand for PAR for further photosynthesis. In the case of ascent, this acclimation reduces the possible self-shading related inter-cellular competition for light with low-carbon cells.

As in LJK, for a cell having internal carbon concentration between  $Cn_{High}$  and  $Cn_{Full}$ , a PAR threshold,  $I_{th}$ , of  $17.5 \mu\text{mol quanta m}^{-2} \text{ s}^{-1}$ , an additional internal carbon threshold at 80% of the range between the minimum and maximum carbon concentration and an internal nitrogen threshold at 90% of the range are used to control its swimming direction. If the cell is exposed to PAR intensity less than  $I_{th}$ , it continues to ascend; otherwise, unless it has both the internal carbon concentration less than the 80% threshold and the internal nitrogen concentration greater than the 90% threshold resting at current depth, it becomes a nitrate-seeking cell. The modification of the swimming orientation model for cells in this category (i.e.,  $Cn_{High} \leq Cn < Cn_{Full}$ ) is also under the control of ambient nitrate condition only for the nitrate-seeking cells. The modified control is exactly the same as that introduced above for the very high carbon cells ( $Cn \geq Cn_{Full}$ ) and is not restated here.

For the dark period, the only modification to LJK is that the ambient nitrate gradient threshold ( $GRAD[\text{NO}_3]_{ori}$ ) is again a criterion for determining a cell's swimming orientation. If a cell's ambient gradient is downward or less than the threshold, the cell descends to seek higher nitrate concentration; otherwise, the cell ascends to seek a depth with higher nitrate concentration. The swimming speed is given as in LJK (see Eq. [A28]), though the sign is positive for ascent and negative for descent. The swimming rules are given in Table A2.

## Reproduction submodel

In our present model, only the least equal daughter reproduction strategy proposed by LJK is considered. The reproduction period is set from 03:00 through 06:00 h as in LJK. This completes the introduction of the model structure.

## Model simulations

The model investigates the influence of different external nitrate conditions which may be experienced by the alongshore filament of *Gymnodinium breve* cells being advected onshore across the west Florida shelf on its bloom development. Since a *G. breve* red tide may take about a month or so to develop into a fish-killing intensity ( $1$  to  $2.5 \times 10^5$  cells  $\text{l}^{-1}$ ), a length of 30 d is chosen for all simulations considered in this paper (Tester & Steidinger 1997, Steidinger et al. 1998). If a constant onshore horizontal velocity of  $3 \text{ cm s}^{-1}$  is assumed, the filament covers a horizontal displacement of about 78 km over a 30 d period. Because *G. breve* blooms usually start offshore in the zone of initiation 18 to 74 km offshore of central Florida, a 78 km horizontal displacement of the filament over the shelf is a reasonable distance for simulating the dynamics of a *G. breve* bloom. In reality, the speed of an onshore current may be time- and space-dependent, and thus the time that an advected *G. breve* population spends in different regions on the shelf may be different. The water depth of the simulation is assumed constant at 15 m.

As mentioned earlier, the nitrate inputs from offshore, mid-shelf and coastal upwellings, *Trichodesmium*-released surface nitrate (proxy for DON) sources associated with ocean fertilizing, multi-nutrient, airborne dust, and a coastal surface plume are all candidates to trigger and/or support *Gymnodinium breve* blooms. Several different time-dependent vertical nitrate distribution patterns are constructed to represent these possible nutrient sources and their spatial and temporal distribution patterns over the west Florida shelf. In the simulations, the nitrate input patterns and associated nitrate concentrations, are constructed according to our sparse observations. These patterns and concentrations can be changed in the future when more data become available from the ECOHAB: Florida Project (Anderson 1995). However, the concentrations set for the simulations cover a range from very low external nitrate concentration ( $0.1 \mu\text{M}$ ) through high concentration (about  $5.0 \mu\text{M}$ ) relative to *G. breve* nitrate uptake determined by Michaelis-Menten kinetics with the half-saturation concentration of  $0.42 \mu\text{M}$  and a  $V_{max}$  as given by Eq. (A20) (see LJK

for the details). These nitrate conditions support 19.2% of the potential maximum uptake rate for 0.1  $\mu\text{M}$  at the low end and 92.3% of the potential maximum uptake rate for 5.0  $\mu\text{M}$  at the high end.

Fig. 2 gives the vertical profiles of all the individual nitrate sources or patterns utilized for the simulations: (1) background oligotrophic pattern; (2) a surface source assumed to be associated with *Trichodesmium* fixation and leakage; (3) upwelled sources, including offshore, mid-shelf, and coastal upwelled sources; and (4) a coastal surface plume. Their formulae are given below. They are used as basic components to construct time-dependent nitrate scenarios (introduced later in this section) for the simulations. Note that  $z$  is positive upwards with  $z = 0$  at the surface; in formulae below,  $z$  is scaled by 1.0 m and thus dimensionless. The vertical profile of the constant, vertically uniform, oligotrophic background component as a basic component present in every scenario is:

$$[\text{NO}_3(z)]_{\text{bgd}} = 0.10 \mu\text{M} \quad (10)$$

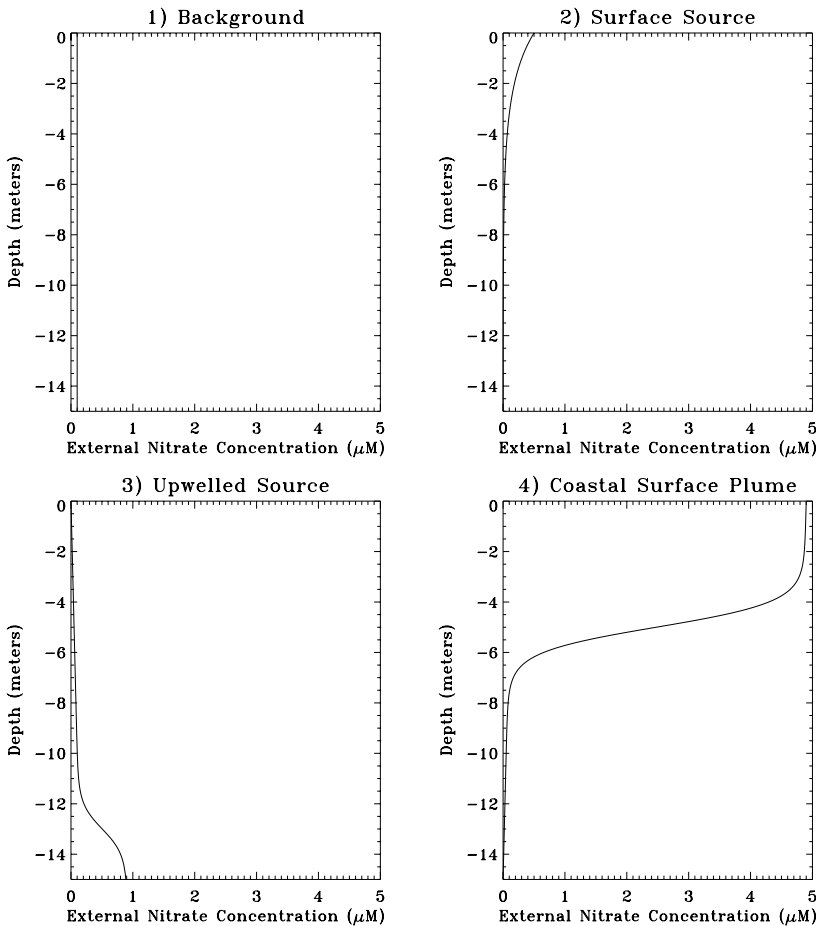


Fig. 2. Vertical profiles of (1) vertically uniform background nitrate condition and (2–4) 3 types of nitrate input patterns at their full strengths, used as components to construct nitrate availability scenarios for simulations.

The vertical profile of the surface source associated with *Trichodesmium* sp. is:

$$[\text{NO}_3(z)]_{\text{surface}} = 0.5 \exp(z/2.0) \mu\text{M} \quad (11)$$

Its maximum concentration is 0.5  $\mu\text{M}$  at the surface and the value of its vertical gradient is greater than the threshold of 0.01  $\mu\text{M m}^{-1}$  (down to 6.4 m below the surface). The intensity of the surface source is relatively low compared to the other sources (see below). The vertical profile of the upwelled sources is:

$$[\text{NO}_3(z)]_{\text{upwelling}} = -0.01z + 0.75[1.0 + \tanh(-z - 13.0)]/2.0 \mu\text{M} \quad (12)$$

where the first term produces a downward vertical nitrate concentration gradient greater than 0.01  $\mu\text{M m}^{-1}$ . The maximum concentration is 0.9  $\mu\text{M}$  at the bottom. This same vertical profile is used for all the upwelled sources considered in the simulations. The vertical profile of the coastal surface plume component is given by:

$$[\text{NO}_3(z)]_{\text{plume}} = 0.01(15.0 + z) + 4.75 [1.0 + \tanh(z + 5.0)]/2.0 \mu\text{M} \quad (13)$$

where the first term produces an upward vertical nitrate concentration gradient greater than 0.01  $\mu\text{M m}^{-1}$  which can be sensed throughout the water column. The maximum concentration is 4.9  $\mu\text{M}$  at the surface. Only in this coastal plume source, does nitrate concentration exceed the threshold for swimming orientation control,  $[\text{NO}_3]_{\text{thr}}$ , of 1.26  $\mu\text{M NO}_3\text{-N}$ , which is located at the base of the plume about 5.5 m below the surface.

During the 30 d simulation period, the vertical nitrate distribution experienced by a *Gymnodinium breve* population is specified to change from one pattern to another. The vertical nitrate distribution experienced by the population at any given moment is the combination of the background concentration component and 1 or more of the 3 other basic components introduced above. Fig. 3 sketches 10 different scenarios which are constructed from the basic components (Fig. 2): (a) offshore upwelling (shorthand as O\_UP); (b) persistent upwelling (P\_UP); (c) coastal surface plume (PL); (d) surface source (SC); (e) offshore upwelling + coastal plume (O\_UP + PL); (f) offshore through mid-shelf upwelling + coastal plume (OM\_UP + PL); (g) per-

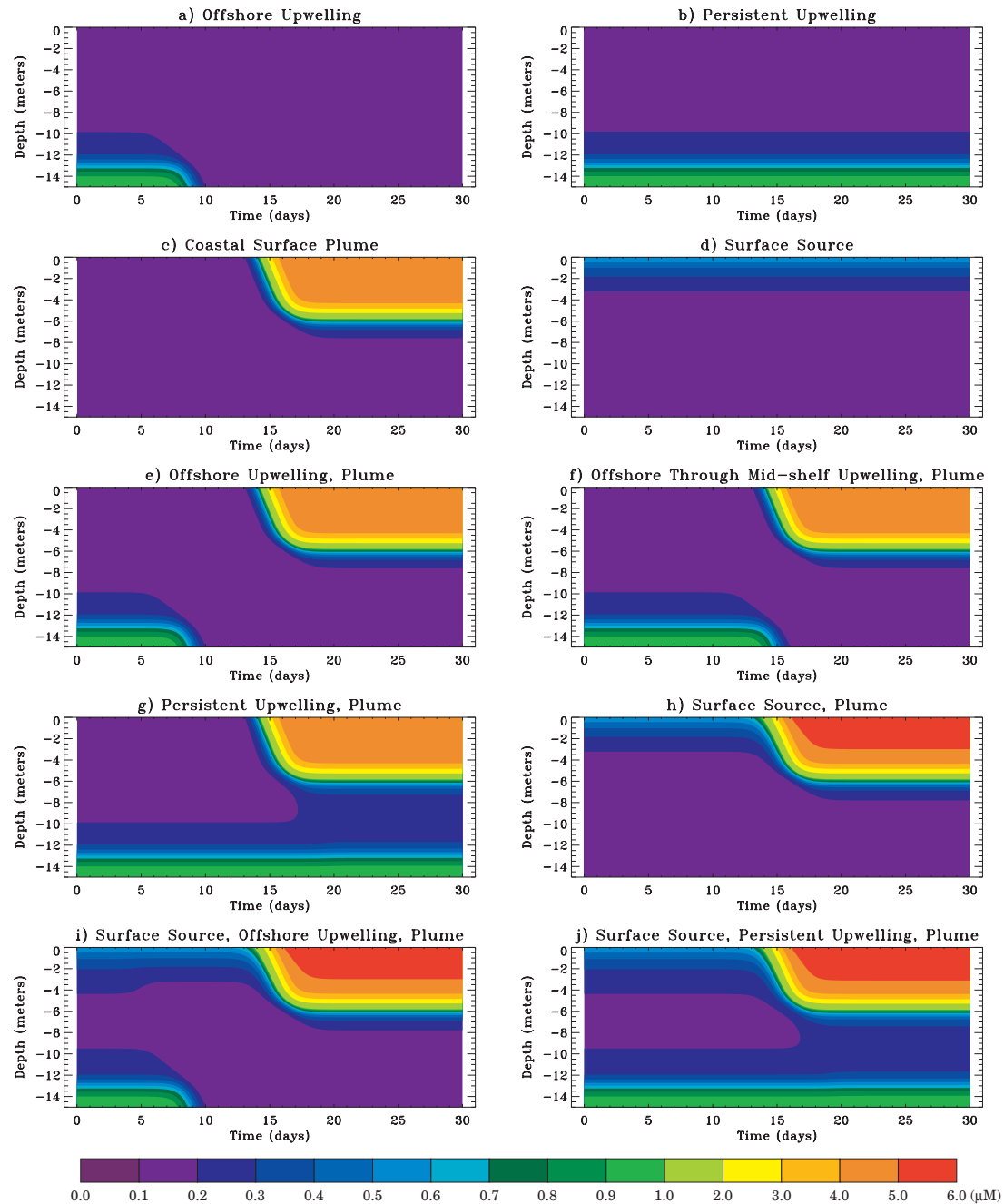


Fig. 3. Ten different nitrate availability scenarios experienced by a filament of *Gymnodinium breve* cells as it moves onshore across a continental shelf over a 30 d period for simulations. Each of the scenarios is composed of the background nitrate concentration and at least 1 of the nitrate input components shown in Fig. 2

sistent upwelling + coastal plume (P\_UP + PL); (h) surface source + coastal plume (SC + PL); (i) surface source + offshore upwelling + coastal plume (SC + O\_UP + PL); (j) surface source + persistent upwelling + coastal plume (SC + P\_UP + PL). The description and mathematical expressions for these scenarios are given in Appendix 2. These scenarios range from con-

taining only 1 nitrate input source, in addition to the background concentration, to containing all the input sources; these 10 scenarios cover the most important nitrate availability patterns known to occur on the west Florida shelf.

A sinusoidal function is used to give the time-dependent PAR intensity for the day. The maximum

PAR intensity at local noon is  $1500 \mu\text{mol quanta m}^{-2} \text{s}^{-1}$ , with sunrise at 06:00 h and sunset at 18:00 h. All the simulations start at 03:00 h on the first day and end at 06:00 h on Day 31. The initial time is chosen at 03:00 h because almost all the reproducing cells divide around 03:00 h during the reproduction period as shown in the LJK simulations and also in our present simulations (not shown). In all simulations, all the *Gymnodinium breve* cells are distributed uniformly through the 15 m deep water column at the initial time with a cell concentration of  $500 \text{ cells l}^{-1}$ , which is a background cell concentration on the west Florida shelf. The initial population consists of 100% fresh daughter cells produced from a quantized parent population (all cells in the starting population divide at the same time) whose cells all have the internal nitrogen pool at the maximum and whose cells are uniformly distributed over 90 through 100% of the internal carbon range between the minimum and maximum value (Kamykowski et al. 1998). The initial biochemical compositions of the daughter cells are distributed from their parents according to the least equal daughter reproduction strategy. The poorer daughter has the minimum level of carbon and nitrogen based on laboratory observations, while the richer daughter cell has the remainder of these components from the mother cell (Kamykowski et al. 1998). The initial photoinhibition is set to 0 for all the cells because at 03:00 h the PAR has been 0 for 9 h. All the cells have the initial 3 d PAR exposure (i.e., sun-shade acclimation) of  $241.5 \text{ quanta m}^{-2} \text{ s}^{-1}$ , which is the mid-point value of the intermediate interval of the five 3 d PAR exposure intervals (introduced below). This initial setting may not be realistic and the simulation results (shown and discussed in the next section) indicate that the cells require a spin-up period of approximately 3 d to adjust their vertical locations and 3 d PAR exposures to their ambient light conditions from their assigned initial values.

The intervals are 15, 20, 20, 5, and 5 for depth ( $z$ ), internal carbon ( $C_n$ ), internal nitrogen ( $N$ ), cumulative inhibition ( $H_c$ ), and 3 d PAR exposure ( $E_3$ ), respectively. Except for the 3 d PAR exposure whose grid spacing is non-uniform to improve resolution (see LJK for the details), the grid spacings for all other variables are uniform. All the grid points are set at the centers of the corresponding discrete intervals. All cells in an interval are considered to have the value at its mid-point (the grid point) but to be uniformly distributed through the length of the interval.

The scale factor ( $SC$ ) of the 3 d simulated PAR exposure calculated by the method discussed in LJK is 2.875 (in LJK under constant light, the scale factor was 1.85) and the range of the 3 d PAR exposure variable is from 0 at a hypothetical infinite depth through about  $521.74 \mu\text{mol quanta m}^{-2} \text{ s}^{-1}$  at the surface for our cur-

rent settings. The same method utilized in LJK is used to discretize 3 d PAR exposure variable axis into 5 non-uniformly spaced intervals. The upper boundaries of the five 3 d PAR exposure reference layers (note that the definition of these layers is different from the definition of the vertical position  $z$  which discretizes the water column) are set at 5 evenly spaced depths:  $ZT = 0, 3.0, 6.0, 9.0,$  and  $12.0 \text{ m}$ , with an additional end point at infinity below the surface. The mid-point values of these intervals are determined by the 3 d PAR exposures at these reference depths with all the initial cells distributed uniformly with depth yielding a uniform value of the light attenuation coefficient. The intervals are centered at 74.6, 176.6, 241.5, 330.3, and 451.6  $\text{quanta m}^{-2} \text{ s}^{-1}$ . This approach gives equal weight to the variable through the vertical domain. All other numerical scheme related settings are the same as in LJK.

For all the simulations, a single time step of 3 min is chosen to satisfy the Courant-Friedrichs-Levy (CFL) numerical stability criterion. The model stores simulation results into data files hourly.

## Simulation results and discussion

In this section, the simulation results of the 10 scenarios are presented and discussed in 3 subsections for the vertical population distribution, final population development, and vertical cellular biochemical distribution, respectively. Most of the figures are plotted from model hourly output.

### Vertical population distribution

Fig. 4 shows the simulated vertical cell concentration distribution and Fig. 5 shows the simulated development of the total population at noon over the 30 d period for the 10 scenarios (a to j). In the simulations, cells take about 3 d (a spin-up period), determined mainly by the sun-shade acclimation with our time scale of 3 d, to adjust their vertical positions and sun-shade acclimation states to the imposed light and nitrate conditions from our more or less arbitrary initial conditions on  $E_3$  (Fig. 4). After the spin-up period, the vertical population distribution is determined primarily by the vertical external nitrate distribution through its influence on *Gymnodinium breve's* diel vertical migration. Under the modelled conditions, HAB concentrations (red:  $10^5 \text{ cells l}^{-1}$ ) are not reached until the end of some simulations.

The simulations show that the surface and bottom are 2 primary locations for cell aggregation, depending on the vertical distribution of external nitrate concentration. Because high nitrate concentration is

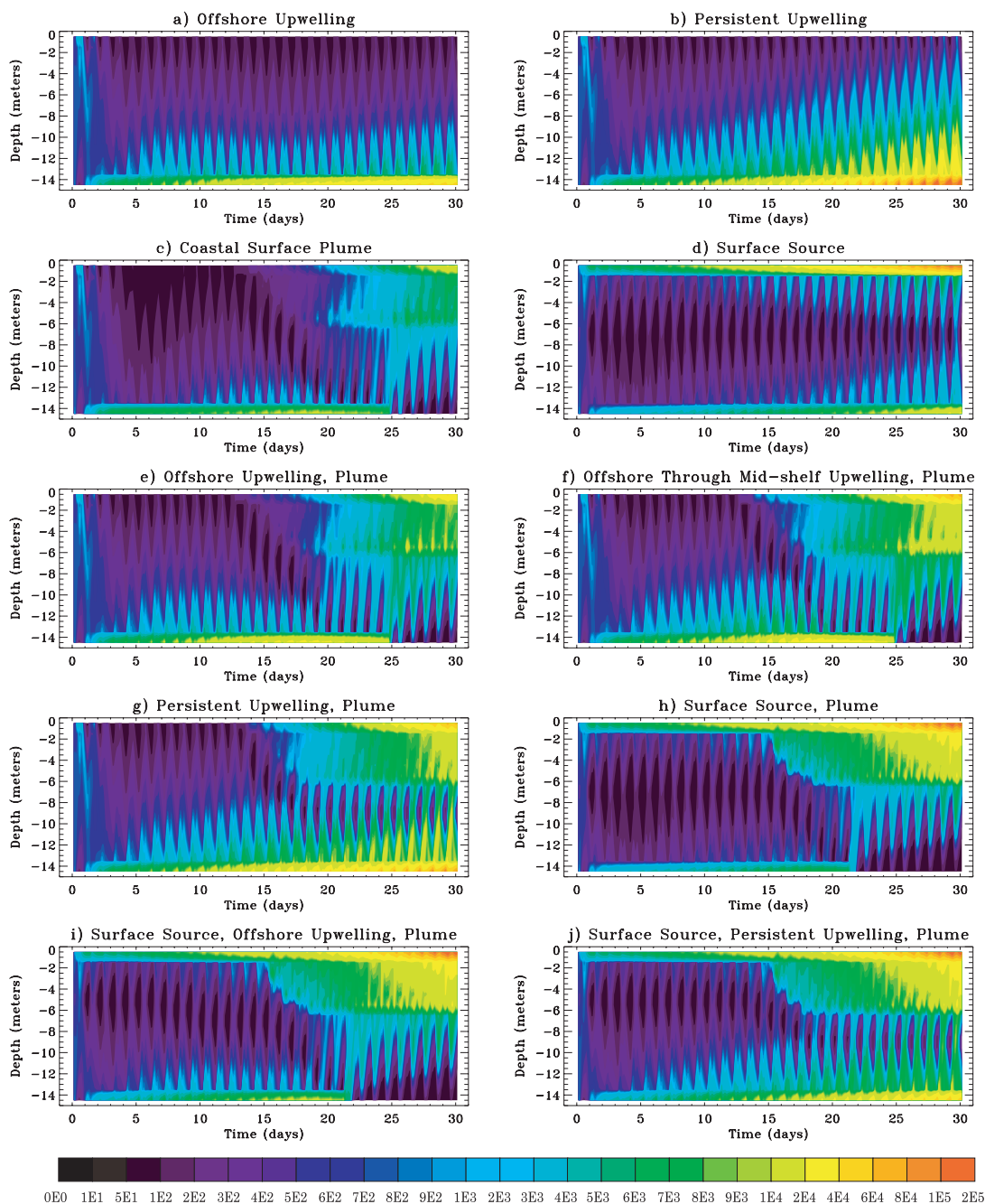


Fig. 4. Simulated vertical cell distribution over a 30 d period for 10 nitrate scenarios (Fig. 3a–j). Bloom levels of  $10^5$  cells  $l^{-1}$  are attained in the orange-red range on the color bar

present either at the surface or at the bottom or at both depths in our simulations and the maximum solar irradiation is at the surface, the aggregations at the surface and/or at the bottom in the corresponding situations are obvious. Vertical gradients of external nitrate concentration of less than  $0.01 \mu\text{M m}^{-1}$  in the lower portion or even in the whole water column is another reason for some simulated bottom aggregations of the

*Gymnodinium breve* cells during the period when both the upwelled sources and coastal surface plume are absent (i.e., in the SC, SC + PL, O\_UP, PL, and O\_UP + PL scenario; Fig. 3a,c,d,e,h). Due to low nitrate gradients, these cells cannot detect if there is elevated nitrate concentration higher in the water column, and hence they seek higher nitrate concentrations at depth. An additional aggregation depth is at the base of the

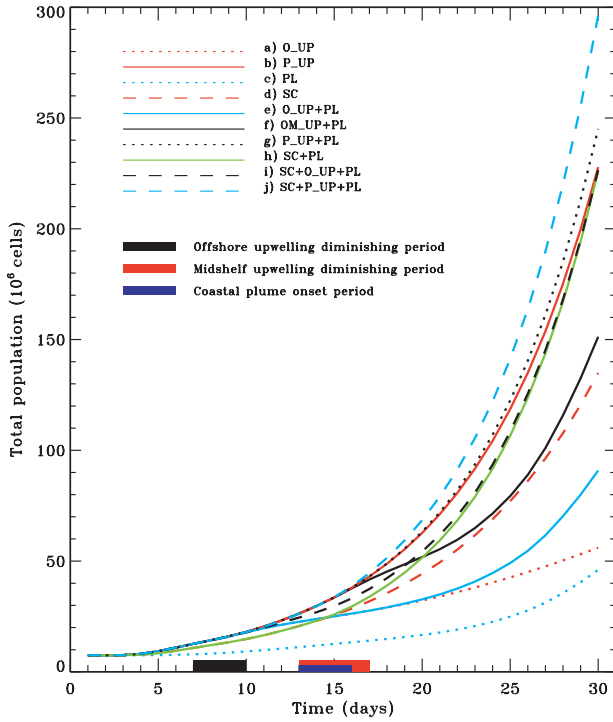


Fig. 5. Simulated population development over a 30 d period for 10 nitrate scenarios (Fig. 3a–j). The curves are plotted using cell numbers at noon of each day

coastal surface plume. Since the nitrate concentration above the plume base (at ~5.5 m below the surface) is greater than  $1.26 \mu\text{M NO}_3\text{-N}$ , high-carbon cells from above may aggregate at this depth during the day and cells from below may aggregate there during the dark period after midnight, according to our swimming rules.

No scenario has a simple single surface or mid-column cell aggregation pattern during any period over the 30 d, although a single bottom aggregation pattern does occur in certain periods of many scenarios (Fig. 4). The concurrence of cell aggregations at 3 depths occurs only during the period when the coastal surface plume coexists with the upwelled source or coexists with the upwelled source in the immediate past. The cell aggregations at the surface and bottom are very persistent and the aggregation at the base of the coastal surface plume is a diel pattern. Table 1 lists

Table 1. Simulated population size, maximum cell concentration, and its timing and depth on the last day (Day 30) of the 30 d period for the 10 scenarios. The time when a maximum cell concentration occurs is in the parentheses beneath the respective cell concentration. The full names of the 10 abbreviated scenario names are: (a) O\_UP: offshore upwelling; (b) P\_UP: persistent upwelling; (c) PL: coastal buoyancy plume; (d) SC: surface source; (e) O\_UP + PL: offshore upwelling + coastal plume; (f) OM\_UP + PL: offshore through mid-shelf upwelling + coastal plume; (g) P\_UP + PL: persistent upwelling + coastal plume; (h) SC + PL: surface source + coastal plume; (i) SC + O\_UP + PL: surface source + offshore upwelling + coastal plume; (j) P\_UP + SC + PL: persistent upwelling + surface source + coastal plume. Note that all the scenarios include the background nitrate concentration. 'Min' and 'Max' columns show the minimum and maximum values, respectively, of the regional maximum cell concentration at the corresponding aggregation depth during the 24 h. Time is shown in parentheses. 'Max1' and 'Max2' columns show the maximum cell concentrations of 2 different cell aggregations both occurring at the base of the plume but at different times of the day: 1 in the morning and 1 in the afternoon, respectively. –: indicates that there is no regional maximum cell concentration at the respective depth

Nutrient scenario	Total population ( $10^6$ cells)	Maximum cell concentration ( $10^3$ cell $\text{l}^{-1}$ )					
		Surface		5.5 m		Bottom	
		Min	Max	Max1	Max2	Min	Max
a. O_UP	56.07	–	–	–	–	42.04 (18:00)	53.82 (04:00)
b. P_UP	227.86	–	–	–	–	90.83 (12:00)	191.22 (04:00)
c. PL	46.01	16.52 (18:00)	22.41 (09:00)	6.13 (04:00)	5.72 (18:00)	–	–
d. SC	134.86	90.35 (14:00)	109.07 (07:00)	–	–	16.86 (11:00)	23.57 (04:00)
e. O_UP + PL	90.88	32.23 (17:00)	44.03 (09:00)	12.76 (04:00)	11.00 (18:00)	–	–
f. OM_UP + PL	151.26	55.51 (18:00)	76.47 (09:00)	19.76 (04:00)	17.86 (18:00)	–	–
g. P_UP + PL	245.06	50.01 (18:00)	69.31 (09:00)	14.17 (04:00)	16.46 (18:00)	52.53 (12:00)	104.38 (04:00)
h. SC + PL	225.93	97.89 (18:00)	136.23 (09:00)	–	24.99 (18:00)	–	–
i. SC + O_UP + PL	226.49	96.74 (18:00)	134.65 (09:00)	–	25.16 (18:00)	–	–
j. SC + P_UP + PL	296.11	95.46 (18:00)	133.13 (09:00)	–	26.38 (18:00)	34.13 (12:00)	65.17 (04:00)

minimum and maximum cell concentrations at the surface, bottom and base of the plume, the times of their occurrences, and the population size on the last day (Day 30) for all the scenarios. The occurrence, vertical location, and intensity of cell aggregation vary between scenarios and with time during the 30 d period depending primarily on vertical nitrate distribution.

In the model, only the low-carbon cells, among the cells at the bottom previously attracted there due to the weak vertical gradient of external nitrate concentration, can ascend back into a possible surface source by seeking higher light exposure. The ascent of lower light-adapted, low-carbon cells from the bottom or a lower portion of the water column is suppressed by photoinhibition initially, but any excursion toward the surface causes these cells to become adapted to a higher light intensity, become less photoinhibited and rise closer to the surface over the time.

Because the nitrate concentration in all the input sources except in the coastal surface plume is less than  $1.26 \mu\text{M NO}_3\text{-N}$ , migration controlling rules do not allow for the population to aggregate away from the surface or the bottom. As a result, the population aggregations during similar time periods are more intense in scenarios without a coastal plume than in scenarios with a coastal plume even though the total population size is about the same in both scenarios. When only an upwelled source is present (i.e., in the O\_UP, P\_UP, O\_UP + PL, OM\_UP + PL, and P\_UP + PL scenario, Fig. 3a,b,e–g), cell aggregation occurs only at the bottom, but low-carbon cells (only a small percentage of the population) ascend during the day looking for higher light exposure. With population development, the number of the ascending low-carbon cells increases over the time. This upwelled nitrate source condition has the most intensive aggregation.

The surface aggregation is most persistent throughout 24 h when the surface nitrate source associated with *Trichodesmium* sp. occurs without the coastal surface plume. The descent of a very small portion of the population may be due to photoinhibition-induced descent caused by high photoinhibition related to a calculation artifact associated with numerical diffusion (LJK).

During the period with bottom cell aggregation, the daily maximum bottom aggregation occurs at 04:00 h in the morning (Table 1) and is caused by the descent of nitrate-seeking cells at night until 04:00 h when overnight nitrate-seeking stops for all the cells according to our swimming rules. The descent continues until 04:00 h because cells are not exposed to ambient nitrate concentration higher than the threshold of  $1.26 \mu\text{M NO}_3\text{-N}$ . The timing of the daily minimum cell concentration at the bottom varies between scenarios and may be determined by the combined result of ascent for light and photoinhibition induced decent

during the day. However, the relative cell concentration achieved during aggregation is also determined by population size (Table 1). We will examine the combined quantitative results later in this section.

During the period when the coastal surface plume is present (7 out of the 10 scenarios, Fig. 4c,e–i), the ambient nitrate-controlled migration allows the high-carbon cells in the population to spread vertically within the plume as determined by the threshold of  $1.26 \mu\text{M NO}_3\text{-N}$  located at the base of the plume about 5.5 m below the surface. Cells aggregate both at the surface (low-carbon cells) and at the base of the plume at 5.5 m (high-carbon cells) and spread out in-between. The cell aggregation during these coastal plume periods is weakest compared with the non-coastal plume periods with similar total population size. When there is not a concurrence of a bottom input source (Scenario c, e, f, h, and i), the bottom cell aggregation is absent because the vertical nitrate concentration gradient is greater than the  $0.01 \mu\text{M m}^{-1}$  sensory threshold throughout the water column. With or without the coexistence of bottom cell aggregation, the plume base aggregation and the surface aggregation exist simultaneously usually with the maximum plume base cell concentration about  $1/5$  to  $1/4$  of the maximum surface concentration during the day (Table 1). In the case without a bottom nitrate input, some cells still descend into the depths below the plume (Fig. 4c,e,f,h,i) during the day. These cells may be new low-carbon daughter cells from the parent cells which were previously within the plume but near the base of the plume and adapted to a relatively low light intensity.

The aggregation at the base of the coastal surface plume is ephemeral within the diel pattern. Two totally different swimming control mechanisms are responsible for aggregations that appear twice (at about 04:00 and 18:00 h) daily with different intensities. For the first aggregation at the base of the plume, some of high-carbon descending cells arrive during the day where the nitrate concentration is  $1.26 \mu\text{M NO}_3\text{-N}$ . This cell aggregation may not be distinguishable if cell concentration in the rest of the plume is high. This maximum cell concentration usually occurs at 18:00 h (sunset) at the end of the photosynthesis period when the internal carbon content of the population is at its highest during the day. This subsurface activity is also why the corresponding daily minimum surface cell concentration (Table 1) occurs at this hour. After sunset, the nighttime swimming control mechanism becomes active, and all of the cells ascend in the plume and the plume base cell aggregation disappears after a few hours. The second aggregation at the base of the plume occurs between midnight through 04:00 h (the nominal resting period; see LJK migration submodel for the details), when the ambient nitrate concentration

of the cells below the base of the plume do not reach the nitrate concentration threshold of  $1.26 \mu\text{M NO}_3\text{-N}$ . Hence, these cells do not rest but continue to ascend across the interface, and then rest at the base of the plume. According to the nighttime swimming speed acclimation mechanism, these aggregating cells are mostly of low-nitrogen type based on the relationship that lower internal nitrogen yields faster ascent speed. This aggregation starts at midnight and maximizes around 04:00 h (at the end of the resting period) and is usually stronger than the first plume-base aggregation at 18:00 h (Table 1). This aggregation also is enhanced by cell reproduction, which occurs mostly right after 03:00 h at this depth and below. This aggregation quickly dissipates after 04:00 h due to the ascent of the low-carbon and/or high-nitrogen cells in the aggregation. The simulated statistical results show that, at 04:00 h, this mid-depth level (5.5 m) contains the highest number of low-carbon cells of any depth level. These low-carbon cells may be the fresh daughter cells or relatively young cells from the previous day's reproduction. The quick ascent of the low-carbon cells from the base of the plume, together with the cells from other depths, induces the daily surface maximal aggregation at about 09:00 h (Table 1).

The most complex vertical cell distribution patterns occur during transition periods between different external nitrate patterns like all of the scenarios with the coastal surface plume. Right after the onset of the coastal surface plume (Days 14 and 15), the cells previously aggregating at depth are not immediately ready for higher nitrate uptake within the plume depth because photoinhibition forces these ascending low light-adapted cells back to depth. In the model, it takes more than 3 d for these previously lower light-adapted cells to become the surface light-adapted cells. On the other hand in the scenarios that also contain the offshore surface source associated with *Trichodesmium* sp., *Gymnodinium breve* cells are all immediately able to conduct nitrate uptake with higher rates in the coastal plume because they have been surface light-adapted.

Although natural *Gymnodinium breve* cells are more concentrated in the surface waters, they are routinely distributed throughout the water column down to >50 m depths. *G. breve* can occur in high concentrations down to 40 m depth. The maximum cell concentrations of *G. breve* have been found at various depths in the water column under bloom conditions (Steidinger & Ingle 1972, Heil 1986). On many occasions they remain at depth throughout the light period with no high surface cell concentrations (Odum et al. 1955) and on other occasions discernible cell concentrations have been found at different depths (Steidinger et al. 1966). Our simulations show that the vertical location of the maximum cell concentration can be associated with the

vertical distribution of external nitrate concentration. A persistent surface maximum throughout the dark period has been found in bloom conditions (Heil 1986). The simulations of the scenarios containing the coastal surface plume and/or the surface source show similar persistent surface maximum cell concentrations both day and night. The coexistence of the coastal surface plume and the surface nitrate source enhances the magnitude of the surface maximum cell concentration.

The simulated strong surface aggregations at night may not be generally realistic, although strong surface aggregation has been observed in the natural blooms during the dark period (Heil 1986). This may also be true for the simulated strong bottom aggregations during the day and/or night. The present swimming rules in the model focus on the migration control over the full water column and the refinement of the rules for a finer structure of vertical cell distribution within a nitrate source may be needed in the future when more relevant field observations become available.

The simulated maximum cell concentrations of all the scenarios reached on the last day (Day 30) are given in Table 1 with the final population sizes listed along for comparison. Six (Scenarios b, d, g, h, i, and j) of the 10 scenarios predict cell concentrations exceeding the fish-killing level of  $10^5 \text{ cell l}^{-1}$ . Two of them have fish-killing cell concentrations at the bottom (Scenarios b and g) and the other 4 at the surface (Scenarios d, h, i, and j). The simulations indicate that a fish-killing *Gymnodinium breve* red tide may take about a month or so to develop from an initial cell concentration of  $500 \text{ cells l}^{-1}$ , which is in the range of the background cell concentration on the west Florida shelf ( $<1000 \text{ cells l}^{-1}$ ), depending on the nitrate support pattern on the shelf. Table 1 also shows that aggregation at the base of the plume in all the scenarios does not reach the fish-killing level in 30 d and a longer time may be required for the presence of fish-killing red tide concentration there. On Day 30 in all 6 of these scenarios, the minimum cell concentration at the depth where the fish-killing cell concentration occurs is just a little below the level of  $10^5 \text{ cell l}^{-1}$  (Table 1); this indicates that the simulated bloom concentration persists throughout the 24 h period. The dates when the fish-killing concentrations appear are Day 27, 30, 30, 28, 28, and 28 for Scenarios b, d, g, h, i, j, respectively.

In general, continuous nitrate availability supported in offshore, mid-shelf and through the coastal regions is required for a population to develop into a fish-killing red tide in 30 d. The influence of the nitrate input pattern on the total population development is discussed in the next subsection. The simulation results, however, also demonstrate that, in addition to supporting population growth, nitrate input pattern also plays a critical role in determining vertical cell dis-

tribution and the intensity of cell aggregation through its influence on *Gymnodinium breve* swimming behavior. The occurrence of more than 1 nitrate input source at different depths may segregate small portions of the total population into different regions of the vertical water column (Fig. 4). Hence, the maximal local cell concentration may be diluted compared to a water column with only a single nitrate source where the cell population can concentrate (Table 1). A good example is the SC + P\_UP + PL scenario versus the P\_UP scenario: the former has largest integrated population size due to more available nitrate on the shelf and higher nitrate concentration in the system, but the latter has the highest local aggregated cell concentration among the scenarios. A comparison of the SC + P\_UP + PL and the SC + PL scenario shows a similar pattern. Behavioral aggregation may thus yield red tide, fish-killing cell concentrations in a localized region of the water column although the cell number integrated through the water column is sub-maximal.

In the 4 scenarios (Scenarios d, h, i, and j) with the surface maximum cell concentration reaching  $10^5$  cell  $l^{-1}$  level, the light attenuation coefficient at the surface depth level increases from initial  $0.1 \text{ m}^{-1}$  to 0.29, 0.33, 0.32, and  $0.32 \text{ m}^{-1}$ , respectively, on the last day. Thus self-shading is in effect for these scenarios. A light attenuation coefficient of  $0.25 \text{ m}^{-1}$  in a *Gymnodinium breve* bloom was reported by Heil (1986) and our simulated values are comparable to this observed value. At local noon on the last day, the PAR intensity at the bottom depth level in the SC + PL scenario, which has the highest surface cell concentration among all the scenarios during the day, is  $206.7 \mu\text{mol quanta m}^{-2} \text{ s}^{-1}$ ; the PAR intensities at 07:00 h (1 h after sunrise) and 17:00 h (1 h before sunset) are 53.7 and 53.2 at the bottom, respectively. Note that, the values at 07:00 and 17:00 h are given here because the model outputs data hourly so 07:00 and 17:00 h are the first and last output time during daylight. Therefore, during the 30 d period PAR intensity through the water column is much higher than the *G. breve* compensation light intensity except during the very short periods just after sunrise and just before sunset, in all the scenarios.

#### Total population development

Fig. 5 shows the total cell number in the water column at noon on each day during the 30 d period for the 10 scenarios and Fig. 6 shows the respective growth

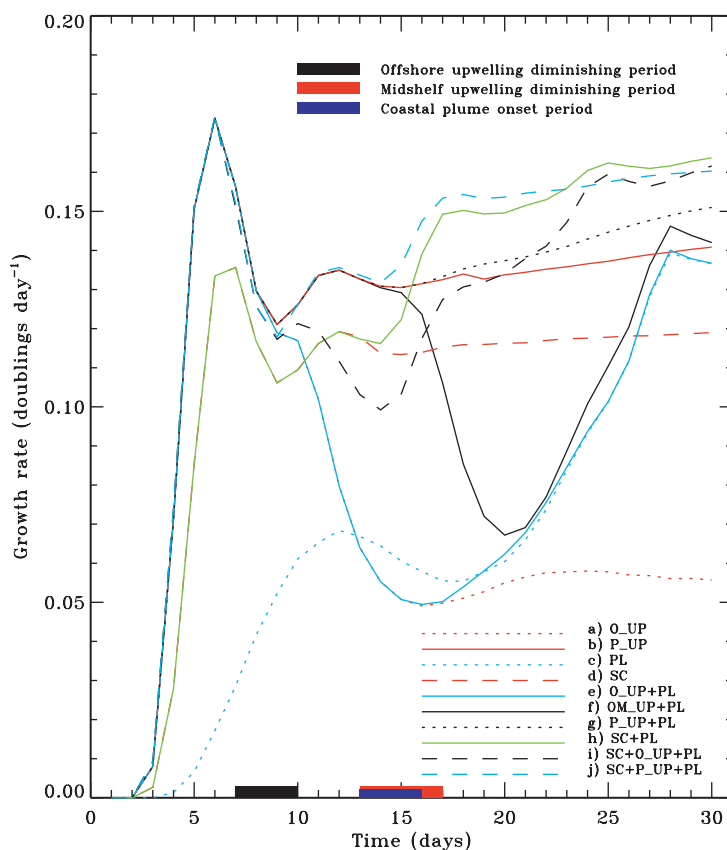


Fig. 6. Simulated daily population growth rate over a 30 d period for 10 nitrate scenarios (Fig. 3a–j). The growth rates are calculated using cell numbers at noon each day

rates calculated on a daily basis. The large variation in the development of the total population over the 30 d period among scenarios indicates the dramatic influence of nitrate input and support pattern on *Gymnodinium breve* population development. The growth rate also varies greatly between scenarios although most of them are similar near the end of the 30 d period.

The population does not reproduce in the first 3 d (Figs. 5 & 6) because all the initial cells are new daughter cells and minimum division interval is 3 d using the nitrate uptake rate specified in the present model (see LJK for the details). After 3 d or so, the cells in the population spread over the whole ranges of the internal carbon and nitrogen and there are always some cells ready for reproduction every day.

The closed black bar and red bar along the x-axis in Figs. 5 & 6 mark the diminishing periods of the offshore and mid-shelf upwelling, respectively. The decrease in the population development is shown clearly in the corresponding scenarios (Scenarios a, e, and i for the offshore upwelling and Scenario f for the mid-shelf upwelling). The closed purple bar marks the onset

period of the coastal surface plume. The increase in population development is shown clearly in the corresponding scenarios (Scenarios c and e–j).

Excluding the SC + PL, SC, and PL scenario, the remaining scenarios have almost the same growth rates for the first 10 d or so (Fig. 6). This is not surprising because all of these scenarios have the offshore upwelled nitrate source during the first 10 d. Some have the surface nitrate source also, but this additional source seems to have little influence on the growth rate (Fig. 6) during the period.

The significant photoinhibition-induced decrease in the population growth rate experienced by populations (Scenarios c, e–j) which contain the coastal surface plume without a prior surface source associated with *Trichodesmium* sp. is again seen here. When a surface nitrate source exists prior to entering the coastal plume (Scenarios h–j), a great number of cells quickly aggregate at the surface, and these cells are ready for higher nitrate uptake in the plume and immediately exhibit high population growth rates.

At the end of the simulations, all the scenarios having the coastal surface plume have very similar population growth rates around  $0.15 \pm 0.015$  doublings  $d^{-1}$ , irrespective of previous nitrate support condition (Fig. 6), but the earlier history of population development plays a dramatic role in determining final population size. The comparison of the population sizes of all the scenarios at the end of the 30 d period demonstrates that the final population size is significantly different between scenarios and greatly determined by the nitrate support over the entire shelf (Fig. 5).

The SC + P\_UP + PL scenario (Fig. 3j) contains all the nitrate input and support sources considered in the model and thus continuously has the largest population size over the course of the 30 d period among the 10 scenarios (Fig. 7, Table 1). The PL, O\_UP, and O\_UP + PL scenario have the smallest population sizes on the last day, because nitrate input source is absent in at least 1 region during crossshelf transport in these 3 scenarios. The nitrate support is absent both in the offshore and mid-shelf region, mid-shelf and coastal region, and mid-shelf region for the PL (the smallest population size), O\_UP (the second smallest), and O\_UP + PL scenario (the third smallest), respectively. Although growth rate of the PL scenario increases rapidly after the onset of the coastal surface plume and catches up with other scenarios in the 30 d, the low initial growth causes its reduced population size.

All of the other scenarios have continuous nitrate support throughout the crossshelf transport. Among them, the SC and OM\_UP + PL scenario have the smaller population sizes. The nitrate concentration of the surface source associated with *Trichodesmium* sp. is the lowest among all the input sources and its depth

range is also the smallest. Carbon production does not play important role in small population size because it is not much different at the surface and bottom for the cells photoadapted to the corresponding depths. Moreover, during the period when only the surface nitrate source exists, a significant number of cells are trapped at the bottom with very low ambient nitrate concentration due to the lack of detectable vertical nitrate gradient. In the OM\_UP + PL scenario, the transition from the nitrate at the bottom to nitrate at the surface between the mid-shelf and coastal region causes the photoinhibition to prevent the low light-adapted *Gymnodinium breve* cells from ascending into the plume. Hence these cells are trapped deep in the water column for a few days without nitrate support and the population growth rate decreases during that period (Fig. 6). The other 4 scenarios (Scenarios b, g, h, and i) have large population sizes because they have more than 1 nitrate input source.

In the SC + P\_UP + PL scenario, the bottom upwelled source with lower nitrate concentration than in the surface plume attracts a significant number of cells at the bottom all the time. Moreover, with the largest population size over the course of 30 d (Fig. 5, Table 1), the self-shading effect is also among the strongest among the 10 scenarios. As a result, although the available nitrate in this system is the highest in the 10 scenarios, the population growth rate becomes lower than the rates of the SC + PL and SC + O\_UP + PL scenarios during the late simulation period (Fig. 6). Although the growth rate of the SC + PL scenario becomes the highest toward the end of the 30 d period, its population size does not become the highest in the 30 d period because of the low population size early in the allotted time period. Thirteen additional days are needed after the end of the 30 d simulation period for the scenario having the lowest population size, i.e., the PL scenario, to catch up with the population size of the scenario having the highest population size, i.e., the SC + P\_UP + PL scenario, assuming that the growth rate keeps constant at about  $0.15$  doublings  $d^{-1}$ .

The simulation indicates that some nitrate support at the initiation stage of the population growth is critical to induce continuous bloom development. On the other hand, without nitrate input in the coastal region, such as the input from a coastal surface plume or coastal upwelling, the growth rate and hence the population development will decrease significantly after the population moves onto the inner shelf. A fully developed bloom is not expected although the growth may already have initiated at an offshore or mid-shelf location, such as in the O\_UP scenario. The simulations also show that, a deep nitrate source in the coastal region may hide the bloom development from a surface observer.

The existence of the maximum growth rate on Day 6 (Fig. 6) is mainly not a nitrate-induced variation. Starting from Day 3 as the minimum division interval, the percentage of the reproducing cells increases daily depending on the availability of nitrate support; this causes the dramatic increase in the growth rate before Day 7. With the increasing growth rate, the percentage of low-carbon cells in the population increases and thus after Day 6 as the percentage of reproducing cells decreases, so does the growth rate. Meanwhile, in the case with the offshore upwelled nitrate input, the new low-carbon cells tend to ascend out of the high nitrate concentration depths at the bottom during the day for photosynthesis. This excursion induces slower nitrate uptake and also lower photosynthetic rate due to higher photoinhibition for these cells. In the case of the surface nitrate source, the increasing surface aggregation intensity due to reproduction reduces the light intensity causing self-shading induced decrease in photosynthetic rate. Hence, the population growth rate decreases after Day 6. The effect of the initial conditions on the growth rate diminishes over the first several days. In most of the scenarios, the growth rate increases again on Days 10 and 11 when the percentage of the reproducing cells increases again.

The maximum growth rate can reach about 0.16 doublings  $d^{-1}$  (Fig. 6). Except for the 'offshore upwelling' scenario which does not support a *Gymnodinium breve* bloom, the growth rates of all other scenarios are within the range approximately between 0.12 and 0.17 doublings  $d^{-1}$  at the end of the simulations. The simulated growth rate is somewhat lower than, but close to, the growth rates of *G. breve* observed in laboratory and field *G. breve* populations, which is typically 0.2 to 0.3 divisions  $d^{-1}$ . However, a fish-killing cell concentration ( $>10^5$  cell  $l^{-1}$ ) is predicted in 6 (Scenarios b, d, g, h, i, and j) of the 10 scenarios. This indicates that even with a relatively low growth rate, a red tide cell concentration can still be developed in about a month, a probable time frame observed in the field (e.g., Steidinger 1973, Tester & Steidinger 1997, Steidinger et al. 1998). Therefore, an 'explosive growth stage' may not be required at all for the development of the *G. breve* red tide.

In Fig. 7 the population size on the last day (Day 30) is plotted against the total amount of the available nitrate in the water column over the 30 d period for all the scenarios. It is interesting to see that the population development is not proportionally related to the total amount of the available nitrate. The pattern of nitrate input, its timing, and duration are more critical for a quick development of a *Gymnodinium breve* bloom than the total amount of the available nitrate.

In Fig. 8, the averaged daily surface cell concentration is plotted versus time. While the total population

development in all cases is fairly uniform with a doubling time of 6 d following Day 15, 4 cases show explosive growth in the surface cell concentration starting with Day 13. These are the cases where there has been no previous surface nitrate support and the surface plume is encountered. In these 4 cases, c, e, f, and g, the surface cell concentrations initially increase by a factor of 10 in 2 d, from Day 13 to 15, and by another factor of 10 over the next 8 d. While the total population increases only by a factor of 3 over this 10 d period, the surface cell concentration increases by a factor of 100. This would be construed by a surface observer as explosive growth; in fact this dramatic increase in surface cell concentration is primarily due to an accumulation of cells near the surface from below the nitrate-rich surface layer.

#### Vertical cellular biochemical distribution

The simulated vertical distributions of the average internal cellular carbon and nitrogen concentration are shown in Figs. 9 & 10, respectively. The vertical distri-

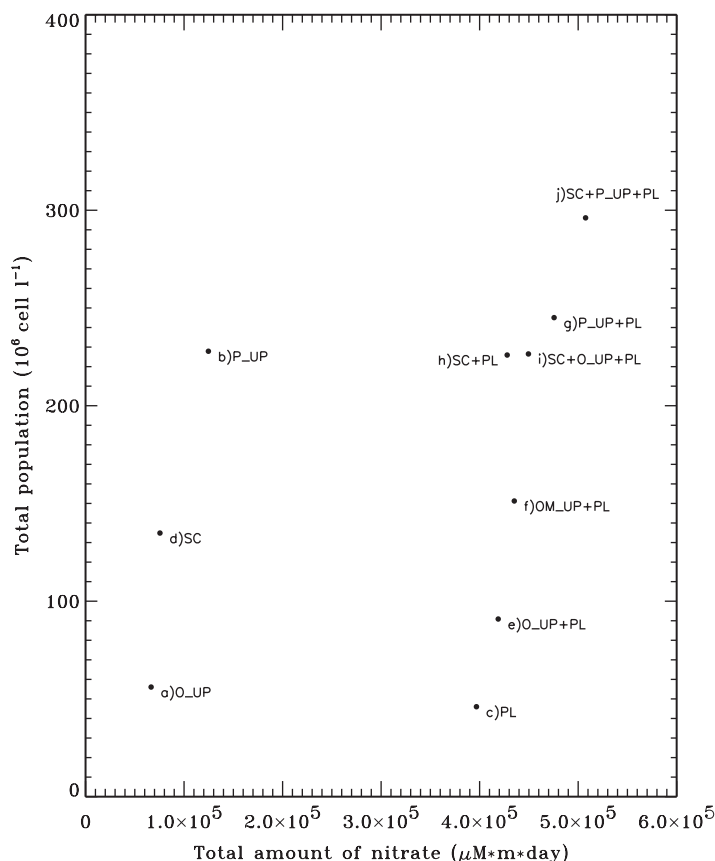


Fig. 7. Simulated population size at noon on the last day (Day 30) against the total amount of available nitrate in the water column over a 30 d period for the 10 nitrate scenarios (Fig. 3a–j)

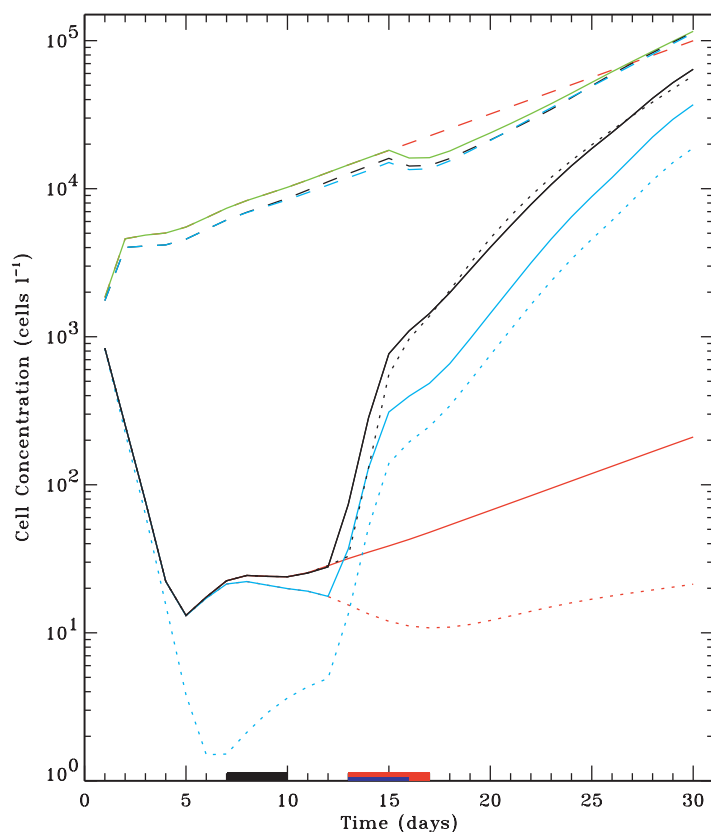


Fig. 8. Simulated surface cell concentrations over a 30 d period for 10 nitrate scenarios (Fig. 3a–j). See Fig. 5 for legend

bution of the average cellular biochemical composition varies greatly between scenarios. These figures need to be examined cautiously because the average internal biochemical concentrations are calculated on per cell basis, and high and low cell densities are given equal weight. Hence, the impression of high average internal biochemical concentration in any region with very low cell concentration may be caused by numerical diffusion of a few cells into a region.

Except for the PL scenario, the vertical distributions of the internal cellular biochemical compositions in the scenarios having only a single nitrate input source, i.e., the O\_UP, P\_UP, and SC scenario (Figs. 9 & 10a,b,d), are very simple, because there is no significant change in the vertical population distribution. In the first 2 of these 3 scenarios, the population aggregates only at the bottom. The average internal carbon and nitrogen concentrations are high in the bottom cells and low in the cells ascending away from the bottom in search of higher light intensity. In the third scenario, the cells aggregate both at the surface and bottom. The surface cells have lower internal carbon but higher internal nitrogen concentrations because the higher reproduction rate in the surface cells yields a population containing a higher percentage of low-carbon new daugh-

ter cells and the surface nitrate source supports the nitrate uptake of the surface cells. The low light-adapted bottom cells have higher internal carbon but lower internal nitrogen concentrations than the surface cells because of the much lower nitrate uptake rate in the oligotrophic water associated with a similar photosynthetic rate as the surface cells.

In all other scenarios (Figs. 9 & 10c,e–j), a common complex pattern is that the vertical distributions of the biochemical compositions change after the transition of the nitrate input pattern during the 30 d period in parallel with the vertical cell distribution. All of these scenarios contain the coastal surface plume. Before the onset of the plume, the bottom is always the location for cell aggregation; hence, the internal biochemical concentrations are always highest in the bottom cells. In the scenarios without the concurrence of the coastal surface plume with the upwelled and/or surface source (Figs. 9 & 10c,e,f), the internal biochemical concentrations in the cells during the plume period are the highest at the base of the plume and lowest in the surface cells. During the plume onset period, the internal biochemical concentrations in the surface cells are higher than the cells at the base of the plume although they are not higher than those in the bottom cells. With the presence of the surface source but without the upwelled source (Figs. 9 & 10h,i), the vertical distributions of the internal biochemical concentrations during the plume period are similar to the scenarios without the surface source (Figs. 9 & 10c,e,f). However, with the presence of the upwelled source (Figs. 9 & 10g,j), the bottom cells during the plume period have the highest average internal biochemical concentrations; the cells at the base of the plume have higher concentrations than the surface cells.

No field data presently are available to compare to the model output. According to the simulations, different vertical cell population and internal biochemical distribution patterns correspond to different vertical nitrate distribution patterns. Collections are underway under the auspices of the ECOHAB:Florida Project (Anderson 1995) to determine if the nitrate and other nutrient concentration patterns, cell population distribution patterns and internal biochemical composition patterns predicted by the different model scenarios occur in nature.

## CONCLUSIONS

The simulation results demonstrate that the diel vertical migration of *Gymnodinium breve* plays a critical role not only in the utilization of natural resources for its population development but also in the population spatial distribution. Furthermore, the environmental nitrate and, by extension, other nutrient distributions

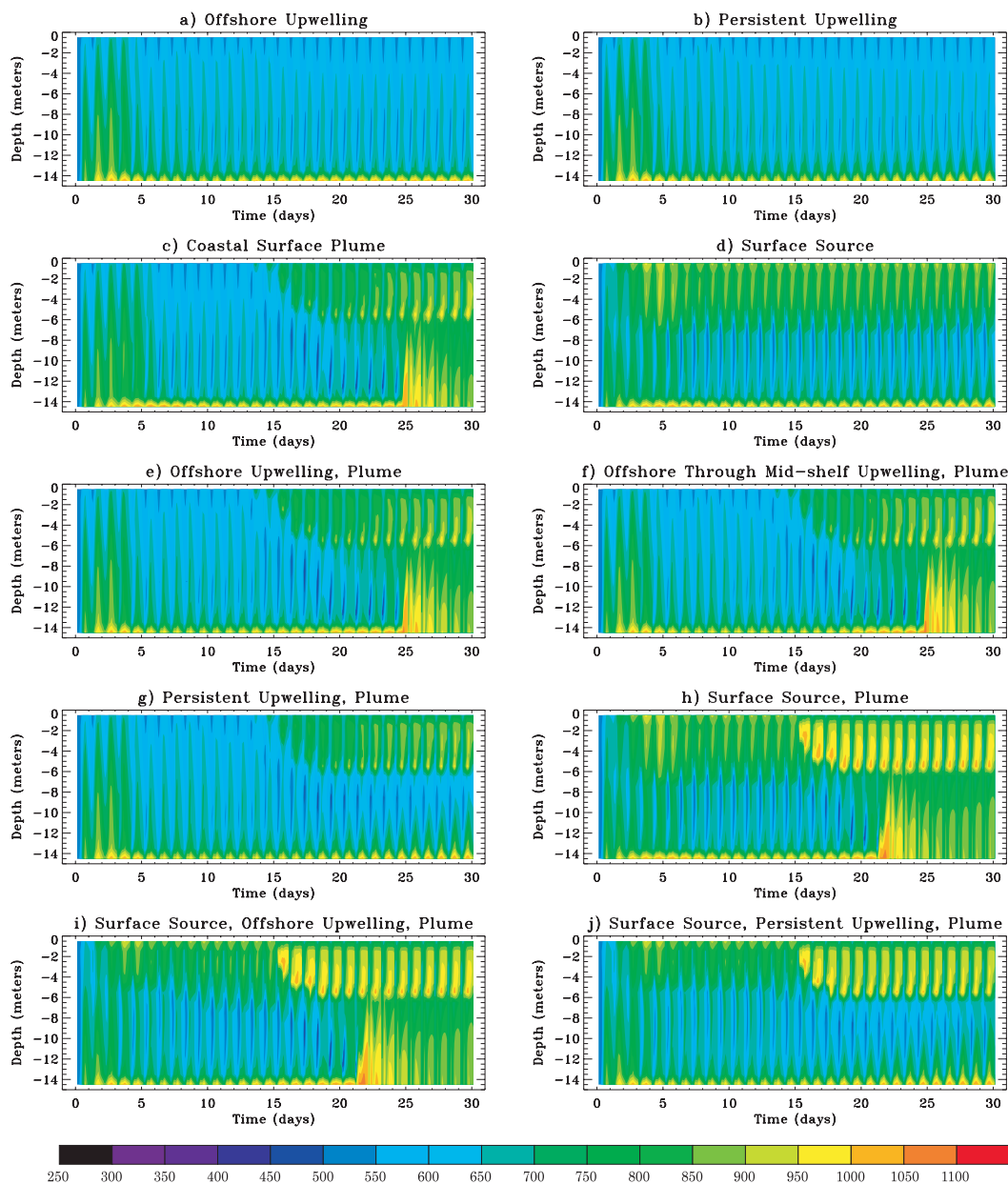


Fig. 9. Simulated vertical distribution of average internal cellular carbon concentration over a 30 d period for 10 nitrate scenarios (Fig. 3a–j)

have a significant influence on *G. breve* population dynamics through its influence on the diel vertical migration of *G. breve*.

Assuming an offshore initiation of the *Gymnodinium breve* bloom, the simulations indicate that the potential nitrate input patterns on the shelf, i.e., offshore, mid-shelf and coastal upwellings, *Trichodesmium* sp.-released surface source associated with multi-nutrient ocean fertilization due to air-borne dust input, and coastal surface plume, are all eligible to trigger and/or support the *G. breve* bloom. However, the oc-

currence, timing, location, duration, and intensity of the bloom are determined by nitrate concentration, input location, and temporal availability. The total amount of the external nitrate available in the water column experienced by the *G. breve* population is important for determining the rate of population development but is not proportionally related to population size.

Some nitrate support at the initiation stage of population growth is very important to induce a continuous development of the bloom, but without additional nitrate input in coastal regions the bloom may not fully

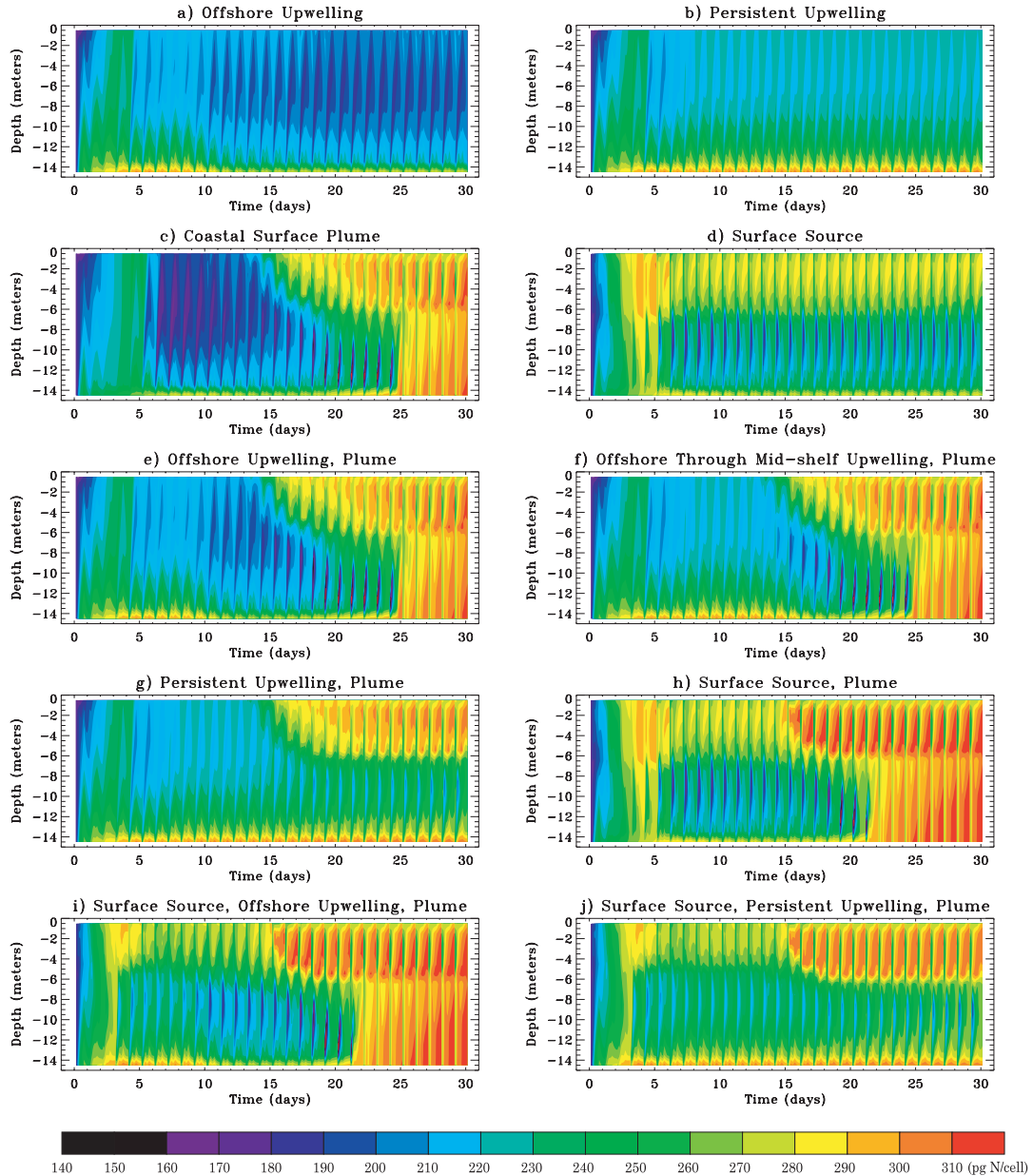


Fig. 10. Simulated vertical distribution of average internal cellular nitrogen concentration over a 30 d period for 10 nitrate scenarios (Fig. 3a-j)

develop. As long as the nitrate is available without interruption from offshore through coastal regions, our simulations show a *Gymnodinium breve* population can develop from the background concentration of  $<1000$  cells  $l^{-1}$  into a fish-killing intensity ( $1$  to  $2.5 \times 10^5$  cells  $l^{-1}$ ) in a month or so, a time frame which has been observed (e.g., Steidinger 1973, Tester & Steidinger 1997, Steidinger et al. 1998), with a maximum growth rate of only about  $0.16$  doublings  $d^{-1}$ . An ‘explosive growth stage’ is not present in the simulations in which fish-killing cell concentrations are developed

in 30 d, but may be an illusion created by the first appearance of high *G. breve* population density at the surface late in bloom development.

The simulations further show that the Expanded Eulerian Method (Janowitz & Kamykowski 1999) is a very useful approach to simulate population dynamics with internal cellular state controlled behaviors. Our list of nitrate availability scenarios is not exhaustive, and the model is capable of being modified to simulate field population more realistically when more field observations become available. In reality, since exter-

nal nutrient availability patterns may be much more complex than presented here, the population distribution may be correspondingly more complicated. More complete observations on the external nutrient condition and its relationship with the population distribution are needed for further simulation and understanding of *Gymnodinium breve* bloom dynamics.

Red tide concentrations of *Gymnodinium breve* may result when dinoflagellates accumulate phototactically during the day through diel vertical migration along downward moving convergences (frontal systems) produced by wind, tide, or current interactions (Donaghay & Osborne 1997, Franks 1997). These vertical lenses may contain between 10 and 100 times their mean concentrations in the water mass in which they are growing (e.g., Seliger et al. 1979). On the other hand, under

intensive vertical mixing in the water column, the role of vertical migration may be much less significant. To further investigate *G. breve* red tide dynamics, realistic 2- and 3-dimensional models, incorporating physical processes including circulation, turbulent mixing, and physical convergence and dispersion and biological processes that integrate *G. breve* into the biological community with which it associates, are needed and our present 1-dimensional *G. breve* population dynamic model serves as a foundation for that purpose.

**Acknowledgements.** We thank Gary Kirkpatrick, Robert E. Reed, and Edward J. Milligan for valuable comments and technical support. This work was supported by ECOHAB: Florida grant funded by the Florida Department of Environmental Protection, NSF grant OCE-95-03253, and NASA grant NAG56586.

**Appendix 1.** This appendix lists all the equations utilized in the model and contains 2 tables: Table A1 listing all the notations and related parameters and their values used in the model and Table A2 summarizing the swimming rules. For details about these equations, see LJK and Model Description section of this chapter. Below, if an equation is followed by 2 equation numbers, the equation is a new equation or a modified LJK equation utilized by our present model, and the second equation number is the number used in the main text of this chapter. If followed by only one equation number, the equation is from LJK unmodified

The governing equation, using the Expanded Eulerian Method (EEM), for the number of identical cells per unit volume,  $C$ , at time  $t$  in  $z$ ,  $Cn$ ,  $N$ ,  $H_c$ , and  $E_3$  space is:

$$\frac{\partial C}{\partial t} + \frac{\partial(V_z C)}{\partial z} + \frac{\partial(V_{Cn} C)}{\partial Cn} + \frac{\partial(V_N C)}{\partial N} + \frac{\partial(V_{H_c} C)}{\partial H_c} + \frac{\partial(V_{E_3} C)}{\partial E_3} = \text{Gains(reproduction)} \quad (\text{A1})$$

The governing equation for the internal cellular carbon during the light period is:

$$V_{Cn} = \frac{dCn}{dt} = -\frac{dCn_{photo}}{dt} - \frac{dCn_{protein}}{dt} \quad (\text{A2})$$

and during the dark period is:

$$V_{Cn} = \frac{dCn}{dt} = -R_m - \frac{dCn_{protein}}{dt} \quad (\text{A3})$$

The governing equation for the internal cellular nitrogen is:

$$V_N = \frac{dN}{dt} = V_{max} \frac{[NO_3(z)]}{K_N + [NO_3(z)]} \quad (\text{A4})$$

The governing equation for the cumulative photoinhibition is:

$$V_{H_c} = \frac{dH_c}{dt} = \frac{H_i - H_c}{\Gamma} \quad (\text{A5})$$

The governing equation for the 3 d PAR exposure is

$$V_{E_3} = \frac{dE_3}{dt} = \frac{I - E_3}{T_3} \quad (\text{A6})$$

The photosynthetic rate, when PAR intensity,  $I$ , is greater than and equal to the PAR compensation threshold,  $I_c$ , is

$$\frac{dCn_{photo}}{dt} = Q \cdot \tanh(E_3) \cdot \left\{ 1.0 - \exp\left(-\frac{I}{I_k} [\tanh(I - I_c)]\right) \right\} \quad (\text{A7, 2})$$

This equation replaces the following equation utilized in LJK where  $I \gg I_c$  and  $E_3 \gg 1$ :

$$\frac{dCn_{photo}}{dt} = Q \cdot \left[ 1.0 - \exp\left(-\frac{I}{I_k}\right) \right]$$

During daylight, when PAR intensity is greater than or equal to 0 but less than  $I_c$ :

$$\frac{dCn_{photo}}{dt} = R_m \cdot \left\{ -1 + \frac{I}{A} + \left(1 - \frac{I_c}{A}\right) \cdot \exp\left[\frac{A+1}{I_c}(I - I_c)\right] \right\} \quad (\text{A8, 3})$$

and

$$Q = [P_{md} + H_c(P_l - P_{md})] \quad (\text{A9})$$

$$A = \frac{Q \cdot \tanh(E_3)}{R_m E_3} I_c^2 + I_c - 1 \quad (\text{A10, 5})$$

$$P_{md} = P_m + P_{mc} \{\sin[(t + \phi)\pi/t_d]\}^3 \quad (\text{A11})$$

$$P_m = P_{ma} + P_{mb} \tanh[(E_3 - a)/b] \quad (\text{A12})$$

Note that, in Eqs. (A7) to (A10),  $E_3$ ,  $I$ ,  $I_k$ , and  $I_c$  have been scaled by  $1 \mu\text{mol quanta m}^{-2} \text{s}^{-1}$  and are dimensionless. The low PAR Eqs. (A8) & (A10) were not needed in LJK. The time dependent, depth varying PAR intensity is given by:

$$I(z,t) = I(0,t) \cdot \exp\left[-\int_z^0 ek(z,t) dz\right] \quad (\text{A13})$$

with the surface PAR intensity

$$I(0,t) = I_{max} \sin[(t + \phi)\pi/t_d] \quad (\text{A14})$$

The chlorophyll  $a$  concentration-dependent total apparent light attenuation coefficient is:

$$ek(z,t) = ek_0 + 0.054 \cdot Chl(z,t)^{2/3} + 0.0088 \cdot Chl(z,t) \quad (\text{A15})$$

A constant average cellular chlorophyll  $a$  content per cell,  $\overline{Chl}$ , of  $42.5 \text{ pg chl } a \text{ cell}^{-1}$  is used to calculate  $Chl(z,t)$  from a cell concentration. The instantaneous photoinhibition is calculated by:

$$H_i = 0 \quad I < I_h \quad (\text{A16})$$

$$H_i = 1.0 - \exp\left[-\frac{(I - I_h)}{I_h}\right] \quad I \geq I_h \quad (\text{A17})$$

## Appendix 1 (continued)

The saturation light intensity and the PAR threshold for inducing instantaneous photoinhibition is determined by:	(internal cellular carbon greater than $Cn_{High}$ , of 68.4 pmol C cell <sup>-1</sup> ) not needed in LJK is:
$I_k = E_3$ (A18)	$V_z = S_{accli} \left\{ 0.2 + 0.8 \left( 1 - \frac{[NO_3(z)]}{K_N + [NO_3(z)]} \right) \right\} \left( \frac{Cn_{max} - Cn}{Cn_{max} - Cn_{High}} \right)^{\frac{1}{2}}$ (A26, 9)
$I_h = 2E_3 + 5$ (A19)	while for the descending high-carbon cells
The internal cellular nitrogen controlled maximum nitrate uptake rate is:	$V_z = -S_{accli} \left\{ 0.2 + 0.8 \left( 1 - \frac{[NO_3(z)]}{K_N + [NO_3(z)]} \right) \right\} \left( \frac{Cn - Cn_{High}}{Cn_{max} - Cn_{High}} \right)^{\frac{1}{2}}$ (A27)
$V_{max} = 5.46e^{-0.186N}$ (A20)	The velocity for the descending (-) or ascending (+) cells during the dark period but more than 2 h from sunrise is:
The maximum nitrogen-in-protein synthesis rate used to calculate carbon-in-protein synthesis is:	$V_z = \pm S_{accli} \left\{ 0.2 + 0.8 \left( 1 - \frac{[NO_3(z)]}{K_N + [NO_3(z)]} \right) \right\} \times$ (A28)
$\mu'_{max} = 0.407 V_{max}$ (A21)	$\left\{ 0.515 \left( 1 + \tanh \left[ 12 - 13.33 \left( \frac{N - N_{min}}{N_{max} - N_{min}} \right) \right] \right) - 0.069 \right\}$
The carbon-in-protein synthetic rate is:	The ascending velocity during the 2 h period prior to sunrise for the low-carbon cells and/or high-nitrogen cells is:
$\frac{dCn}{dt} = 2.0 \cdot \mu'_{max} \left( 1 - \frac{K_q}{0.869 \cdot N} \right)$ (A22)	$V_z = 0.25 S_{accli} \left( \frac{Cn_{max} - Cn}{Cn_{max} - Cn_{min}} \right)$ (A29)
The light-acclimated swimming speed is:	Now, all the equations in the model are described. The last submodel which needs to be mentioned is the reproduction submodel. In our present model, only the least equal daughter reproduction strategy is considered: 1 daughter cell gets the minimum amounts of both internal carbon and nitrogen from its parent and the other gets the remainder of each constituent as determined in Kamykowski et al. (1998). The 2 daughter cells keep the same values of the cumulative photoinhibition and 3 d PAR exposure as their parent cell. The reproduction period is from 03:00 to 06:00 h every day. Reproduction is taken to occur when a cell's internal nitrogen pool is at its maximum, i.e., 23.30 pmol N cell <sup>-1</sup> ( $N_{max}$ ), and its internal cellular carbon pool exceeds 90% of the ranges, i.e., 85 pmol C cell <sup>-1</sup> ( $Cn_{div}$ ).
$S_{accli} = S_{250} \cdot \{ 1 + d \cdot (\tanh[\alpha \cdot I / (d \cdot S_{250})]) - \tanh[\alpha \cdot 250 \mu\text{mola quanta m}^{-2} \text{s}^{-1} / (d \cdot S_{250})] \}$ (A23)	
Note that, in the equation, the first $S_{250}$ is 1 m h <sup>-1</sup> (i.e., 278 $\mu\text{m s}^{-1}$ , Heil 1986) while 278 $\mu\text{m s}^{-1}$ is used in the arguments of the hyperbolic tangent functions.	
During the light period, the ascending velocity for the low-carbon cells (internal cellular carbon less than $Cn_{High}$ , of 68.4 pmol C cell <sup>-1</sup> ) is:	
$V_z = +S_{accli} \left( \frac{Cn_{max} - Cn}{Cn_{max} - Cn_{min}} \right)^2$ (A24)	
The descending velocity for the photoinhibited cells if the extents of their cumulative photoinhibition are greater than 0.8 ( $H_{CSW}$ ) is:	
$V_z = -S_{accli}$ (A25)	
The swimming speed for the ascending high-carbon cells	

Table A1. List of the symbols in the model and their definitions. All the biochemical related variables and parameters are on per cell basis. Note that, in the model computation all other time units are converted into seconds. In the third column of the table, the numbers in '[ ]' give the range of the respective variable values. The '\*' in the definition column indicates the respective variable is an EEM independent variable

Symbol	Definition	Value in the model
$a$	Constant in formula for $P_m$	46.0 $\mu\text{mola quanta m}^{-2} \text{s}^{-1}$
$b$	Constant in formula for $P_m$	17.0 $\mu\text{mola quanta m}^{-2} \text{s}^{-1}$
$\underline{C}$	Number of cells having the same internal states per unit volume in $z$ , $Cn$ , $N$ , $H_c$ , $E_3$ space at a spatial position ( $x, y, z$ ) and at time $t$	Variable, cell per unit volume in $z$ , $Cn$ , $N$ , $H_c$ , $E_3$ space
$Cn$	*Internal cellular carbon, not including $Cn_{protein}$	Variable, [36, 90] pmol C cell <sup>-1</sup>
$Cn_{Full}$	Internal carbon threshold for swimming orientation control	87.3 pmol C cell <sup>-1</sup>
$Cn_{High}$	Internal carbon threshold for swimming orientation control	68.4 pmol C cell <sup>-1</sup>
$Cn_{max}$	Maximum internal cellular carbon	90.0 pmol C cell <sup>-1</sup>
$Cn_{min}$	Minimum internal cellular carbon	36.0 pmol C cell <sup>-1</sup>
$Cn_{photo}$	Net photosynthetic carbon	Variable, pmol C cell <sup>-1</sup>
$Cn_{protein}$	Carbon in the cellular protein	Variable, pmol C cell <sup>-1</sup>
$Chl$	Chlorophyll $a$ concentration in the water	Variable, mg chl $a \text{ m}^{-3}$

Table A1 (continued)

Symbol	Definition	Value in the model
$\overline{Chl}$	Average cellular chlorophyll <i>a</i> concentration	42.5 pg chl <i>a</i> cell <sup>-1</sup>
$d$	A constant for determining swimming speed	0.26, dimensionless
$dt$	Time interval for the numerical scheme	180 s (i.e., 3 min)
$E_3$	*Sun-shade photoacclimation (3 d PAR exposure)	Variable, [0, 522] $\mu\text{mol quanta m}^{-2} \text{s}^{-1}$
$ek$	Chlorophyll <i>a</i> concentration-dependent total apparent light attenuation coefficient	Variable, $\text{m}^{-1}$
$ek_0$	PAR attenuation coefficient due to water alone	0.1 $\text{m}^{-1}$
$GRAD[NO_3]_{ori}$	Threshold of the vertical nitrate concentration gradient for swimming orientation control	0.01 $\mu\text{M NO}_3\text{-N m}^{-1}$
$H_c$	*Cumulative photoinhibition	Variable, [0, 1], dimensionless
$H_i$	Instantaneous inhibition	Variable, [0, 1], dimensionless
$I$	PAR (photosynthetically active radiation) intensity	Variable, [0, 1500] $\mu\text{mol quanta m}^{-2} \text{s}^{-1}$
$I_c$	PAR compensation threshold	6.0 $\mu\text{mol quanta m}^{-2} \text{s}^{-1}$
$I_h$	Sun-shade acclimated PAR threshold for inducing instantaneous photoinhibition	Variable, $\mu\text{mol quanta m}^{-2} \text{s}^{-1}$
$I_k$	Sun-shade acclimated saturation light intensity	Variable, $\mu\text{mol quanta m}^{-2} \text{s}^{-1}$
$I_{max}$	Maximum PAR intensity at the surface	1500 $\mu\text{mol quanta m}^{-2} \text{s}^{-1}$
$I_{th}$	PAR threshold for swimming orientation control	17.5 $\mu\text{mol quanta m}^{-2} \text{s}^{-1}$
$K_N$	Half-saturation constant	0.42 $\mu\text{M NO}_3\text{-N}$
$K_q$	Minimum cellular nitrogen quota for protein synthesis to take place	8.75 pmol N cell <sup>-1</sup>
$N$	*Internal cellular nitrogen	Variable, [6.32, 23.3] pmol N cell <sup>-1</sup>
$N_{max}$	Maximum internal nitrogen	23.30 pmol N cell <sup>-1</sup>
$N_{min}$	Minimum internal nitrogen	6.32 pmol N cell <sup>-1</sup>
$[NO_3]$	External nitrate concentration	Variable, $\mu\text{M NO}_3\text{-N}$
$[NO_3]_{th}$	Ambient nitrate concentration threshold for swimming orientation control	1.26 $\mu\text{M NO}_3\text{-N}$
$P_l$	Light-adapted production rate	0.25 pmol C cell <sup>-1</sup> h <sup>-1</sup>
$P_m$	Sun-shade acclimated maximum photosynthetic rate	Variable, pmol C cell <sup>-1</sup> h <sup>-1</sup>
$P_{ma}$	A constant for determining $P_m$	0.67 pmol C cell <sup>-1</sup> h <sup>-1</sup>
$P_{mb}$	A constant for determining $P_m$	0.25 pmol C cell <sup>-1</sup> h <sup>-1</sup>
$P_{mc}$	Maximum increment of the diel photosynthesis variation	3.33 pmol C cell <sup>-1</sup> h <sup>-1</sup>
$P_{md}$	Dark-adapted production rate	Variable, pmol C cell <sup>-1</sup> h <sup>-1</sup>
$R_m$	Dark carbon respiration rate	0.333 pmol C cell <sup>-1</sup> h <sup>-1</sup>
$S_{250}$	Asymptotic swimming speed acclimated to a light intensity of 250 $\mu\text{mol quanta m}^{-2} \text{s}^{-1}$	1.0 m h <sup>-1</sup> (= 278 $\mu\text{m s}^{-1}$ )
$S_{accli}$	Light-acclimated maximum swimming speed	Variable, m h <sup>-1</sup>
$SC$	Scale factor for $E_3$	2.875, dimensionless
$T_3$	Time scale of the sun-shade acclimated parameters	3 d
$T_{div}$	Cell division time scale	3 d/div
$t$	Time	Variable, second
$t_d$	Length of the daylight hours	12 h
$V_{Cn}$	Change rate of $Cn$	Variable, pmol C cell <sup>-1</sup> s <sup>-1</sup>
$V_N$	Change rate of $N$	Variable, pmol N cell <sup>-1</sup> s <sup>-1</sup>
$V_{Hc}$	Change rate of $H_c$	Variable, s <sup>-1</sup>
$V_{E_3}$	Change rate of $E_3$	Variable, $\mu\text{mol quanta m}^{-2} \text{s}^{-1}$
$V_{max}$	Maximum nitrate uptake rate	Dependent on internal nitrogen content, pmol N cell <sup>-1</sup> h <sup>-1</sup>
$V_z$	Vertical swimming velocity	Variable, m h <sup>-1</sup>
$z$	Vertical coordinate which is 0 at the surface and positive upwards	Variable, m
$ZT_i$	Depth of the upper boundaries of the 3 d PAR exposure reference layers	0, 3, 6, 9, 12 m, and $\infty$
$\alpha$	Initial slope of the curve of light acclimated swimming speed increment	0.55 $\mu\text{m m}^2 \mu\text{mol quanta}^{-1}$
$\Gamma$	Time scale of induction and recovery of the photoinhibition	1.0 h
$\mu'_{max}$	Maximum nitrogen-in-protein synthetic rate	Variable, pmol N <sub>protein</sub> cell <sup>-1</sup> h <sup>-1</sup>
$\phi$	Phase making the maximum value occur at local noon	0 h

Table A2. Hypothesized swimming rules. The threshold values of  $H_c$ ,  $C$ ,  $N$  are the fractions of the ranges between the minimum and maximum values of the respective variables. PAR intensity (i.e.,  $I(z)$ ) is expressed in  $\mu\text{mol quanta m}^{-2} \text{s}^{-1}$ , and  $[\text{NO}_3]$  and  $K_N$  are expressed in  $\mu\text{M NO}_3\text{-N}$ . Changes from LJK are denoted by an asterisk in direction and by speed with 2 equation numbers

Independent variable ranges for swimming orientation control	Swimming direction	Corresponding equation for swimming speed
For the light period (i.e., between 06:00 [sunrise] and 18:00 h [sunset]):		
If $H_c < 0.8$ and		
$C < 0.6$	Up	(A24)
$0.6 \leq C < 0.95$ , and $I(z) < 17.5$	Up	(A24)
$0.6 \leq C < 0.8$ , $N \geq 0.9$ , and $I(z) \geq 17.5$	Rest	–
$0.6 \leq C < 0.8$ , $N < 0.9$ , and $I(z) \geq 17.5$		
$[\text{NO}_3] = 1.26$	Rest	–
$[\text{NO}_3] > 1.26$	Down	(A27)
$[\text{NO}_3] < 1.26$ and ambient $d[\text{NO}_3]/dz \geq +0.01$	Up*	(A26, 9)
$[\text{NO}_3] < 1.26$ and ambient $d[\text{NO}_3]/dz < +0.01$	Down	(A27)
$0.8 \leq C < 0.95$ , and $I(z) \geq 17.5$ :		
$[\text{NO}_3] = 1.26$	Rest	–
$[\text{NO}_3] > 1.26$	Down	(A27)
$[\text{NO}_3] < 1.26$ and ambient $d[\text{NO}_3]/dz \geq +0.01$	Up*	(A26, 9)
$[\text{NO}_3] < 1.26$ and ambient $d[\text{NO}_3]/dz < +0.01$	Down	(A27)
$C \geq 0.95$ :		
$[\text{NO}_3] = 1.26$	Rest	–
$[\text{NO}_3] > 1.26$	Down	(A27)
$[\text{NO}_3] < 1.26$ and ambient $d[\text{NO}_3]/dz \geq +0.01$	Up*	(A26, 9)
$[\text{NO}_3] < 1.26$ and ambient $d[\text{NO}_3]/dz < +0.01$	Down	(A27)
If $H_c \geq 0.8$	Down	(A25)
For the dark period between 06:00 (sunset) and 00:00 h (midnight):		
Ambient $d[\text{NO}_3]/dz \geq +0.01$	Up*	(A28)
Ambient $d[\text{NO}_3]/dz < +0.01$	Down	(A28)
For the dark period between 00:00 (midnight) and 04:00 h:		
$[\text{NO}_3] \geq 1.26$	Rest	–
$[\text{NO}_3] < 1.26$ and ambient $d[\text{NO}_3]/dz \geq +0.01$	Up*	(A28)
$[\text{NO}_3] < 1.26$ and ambient $d[\text{NO}_3]/dz < +0.01$	Down	(A28)
For the dark period between 04:00 and 06:00 h (sunrise):		
$N \geq 0.9$ and/or $C < 0.1$	Up	(A29)
All others	Rest	–

**Appendix 2.** Description and mathematical expressions of the time-dependent vertical nitrate profiles for all 10 nitrate scenarios (Scenarios a–j)

(a) Offshore upwelling: in this scenario, there is only an offshore upwelled nitrate input without mid-shelf and coastal nitrate support. The mathematical expression is:

$$[\text{NO}_3(z,t)]_a = [\text{NO}_3(z)]_{bkgd} + [\text{NO}_3(z)]_{upwelling} \{1.0 - (1.0 + \tanh[t - (4.0 - z/3.0)]) / 2.0\}$$

The time-dependent hyperbolic function here and in other offshore or mid-shelf upwelling scenarios discussed below gives a smooth intrusion shape to the upwelling frontal structure.

(b) Persistent upwelling: this continuous upwelling pattern over the whole 30 d period mimics a population that experiences all 3 possible upwelling events, i.e., the offshore, mid-shelf, and coastal upwelling, as it moves onshore. For the simplicity, these 3 different upwellings are considered having the same intensity and are consecutive to each other:

$$[\text{NO}_3(z,t)]_b = [\text{NO}_3(z)]_{bkgd} + [\text{NO}_3(z)]_{upwelling}$$

(c) Coastal surface plume: this scenario mimics the situation that the population does not run into any high nitrate sources in the offshore and mid-shelf region until it moves into the coastal region where the coastal surface plume is located. The mathematical expression is:

$$[\text{NO}_3(z,t)]_c = [\text{NO}_3(z)]_{bkgd} + [\text{NO}_3(z)]_{plume} \cdot \{1.0 + \tanh[t - (15.0 - z/3.0)]\} / 2.0$$

## Appendix 2 (continued)

The time-dependent hyperbolic function here and in other coastal surface plume containing scenarios introduced below is to give a smooth intrusion shape to the coastal surface plume frontal structure and  $t$  in this equation and the following equations are in the units of days.

(d) Surface nitrate (proxy for DON) source associated with *Trichodesmium* sp.: this is a persistent surface source with a time-independent vertical profile, i.e.:

$$[NO_3(z,t)]_d = [NO_3(z)]_{bkgd} + [NO_3(z)]_{surface}$$

(e) Offshore upwelling + coastal plume:

$$[NO_3(z,t)]_e = [NO_3(z,t)]_c + [NO_3(z)]_{upwelling} \{1.0 - (1.0 + \tanh[t - (4.0 - z/3.0)]) / 2.0\}$$

(f) Offshore through mid-shelf upwelling + coastal plume:

$$[NO_3(z,t)]_f = [NO_3(z,t)]_c + [NO_3(z)]_{upwelling} \{1.0 - (1.0 + \tanh[t - (10.0 - z/3.0)]) / 2.0\}$$

(g) Persistent upwelling + coastal plume:

$$[NO_3(z,t)]_g = [NO_3(z,t)]_c + [NO_3(z)]_{upwelling} + 0.01 \cdot z \cdot 0.5 \{1.0 + \tanh[2.0 \cdot (5.0 + z)]\} \cdot \{1.0 + \tanh[t - (15.0 - z/3.0)]\} / 2.0$$

The additional term on the right-hand side guarantees the vertical nitrate gradient in the coastal surface plume is greater than  $0.01 \mu\text{M m}^{-1}$  because of the offset of the opposite vertical gradients caused by the combination of the upwelled and coastal surface plume components.

(h) Surface source + coastal plume:

$$[NO_3(z,t)]_h = [NO_3(z,t)]_c + [NO_3(z)]_{surface}$$

(i) Surface source + offshore upwelling + coastal plume:

$$[NO_3(z,t)]_i = [NO_3(z,t)]_c + [NO_3(z)]_{surface} + [NO_3(z)]_{upwelling} \{1.0 - (1.0 + \tanh[t - (4.0 - z/3.0)]) / 2.0\}$$

(j) Surface source + persistent upwelling + coastal plume:

$$[NO_3(z,t)]_j = [NO_3(z,t)]_c + [NO_3(z)]_{upwelling} + [NO_3(z)]_{surface} + 0.01 \cdot z \cdot 0.5 \{1.0 + \tanh[2.0 \cdot (5.0 + z)]\} \cdot \{1.0 + \tanh[t - (15.0 - z/3.0)]\} / 2.0$$

The transition time period is about 3 d for the upwellings to vanish; the offshore upwelling starts to diminish on Day 8 and the mid-shelf upwelling on Day 14. The coastal surface plume starts on Day 13 and takes about 5 d to establish fully. The duration of the offshore upwelling is about 9 d; the mid-shelf upwelling is about 6 d; the coastal upwelling is about 15 d; the coastal surface plume is about 15 d, and the surface source associated with *Trichodesmium* sp. is throughout the 30 d period. Here, we assume that the water column moves across the shelf more slowly in the coastal region than in the offshore and mid-shelf regions, or say, within the 30 d the water column spends more time in the coastal region. These are the 10 scenarios constructed for the simulations of the model. The model is sufficiently flexible to simulate other nutrient conditions as they are identified in the field.

Including the background nitrate concentration, the maximum nitrate concentration in the surface source associated with the *Trichodesmium* sp. region is  $0.6 \mu\text{M NO}_3\text{-N}$  (causing 58.8% of the potential maximum uptake rate); in the upwelled source region,  $1.0 \mu\text{M NO}_3\text{-N}$  (70.4%) at the bottom; and in the coastal surface plume region (not including the surface source associated with *Trichodesmium* sp., 5.0 (92.3%) at the surface. The highest nitrate concentration attained among the 10 scenarios occurs in the coastal region in Scenarios h–j where the background low-nitrate concentration, surface source associated with *Trichodesmium* sp., and coastal surface plume co-occur in the coastal region.

## LITERATURE CITED

- Anderson DM (1995) ECOHAB, the ecology and oceanography of harmful algal blooms: a national research agenda. Woods Hole Oceanographic Institution, Woods Hole, MA
- Austin HM, Jones JI (1974) Seasonal variation of physical oceanographic parameters on the Florida middle ground and their relation to zooplankton biomass on the west Florida shelf. Fla Sci 37:16–32
- Chew F (1955) Red tide and the fluctuation of conservative concentrations at an estuarine mouth. Bull Mar Sci Gulf Caribb 5(4):321–330
- Chew F (1956) A tentative method for the prediction of the Florida red tide outbreaks. Bull Mar Sci Gulf Caribb 6(4): 292–304
- Dahl E, Tangen K (1993) 25 years experience with *Gyrodinium aureolum* in Norwegian waters. In: Smayda TJ, Shimizu Y (eds) Toxic phytoplankton blooms in the sea. Elsevier, Amsterdam, p 15–22
- Donaghay PL, Osborne TR (1997) Toward a theory of biological-physical control of harmful algal bloom dynamics and impacts. Limnol Oceanogr 42:1283–1296
- Dragovich A, May BZ (1961) Hydrology of Tampa Bay and adjacent waters. In: Galveston Biological Laboratory fish-

- ery research for the year ending June 30, 1961. US Fish Wildl Serv, Circ, 129
- Dragovich A, Finucane JH, Kelly JA Jr, May BZ (1963) Counts of red-tide organisms, *Gymnodinium breve*, and associated oceanographic data from Florida west coast, 1960–61. US Fish Wildl Serv Spec Sci Rept Fisheries no. 455, iii+40pp
- Duce RA (1986) The impact of atmospheric nitrogen, phosphorus and iron species on marine phytoplankton productivity. In: Buat-Menard P, Reidel D (eds) The role of air-sea exchange in geochemical cycling. Norewell, MA, p 497–529
- Franks PJS (1997) Models of harmful algal blooms. *Limnol Oceanogr* 42:1273–1282
- Geesey M, Tester P (1993) *Gymnodinium breve*: ubiquitous in Gulf of Mexico waters? In: Smayda TJ, Shimizu Y (eds) Toxic phytoplankton blooms in the sea. Elsevier, Amsterdam, p 251–255
- Haddad KD, Carder KL (1979) Oceanic intrusion: one possible initiation mechanism of red tide blooms on the west coast of Florida. In: Taylor D, Seliger H, Lewis C (eds) Toxic dinoflagellate blooms. Proc 2nd Int Conf, Elsevier, New York, p 269–274
- Heil C (1986) Vertical migration of *Ptychodiscus breve* (Davis) Steidinger. MS thesis, University of South Florida, St. Petersburg
- Ikegami S, Imai I, Kato J, Ohtake H (1995) Chemotaxis toward inorganic phosphate in the red tide alga *Chattonella antiqua*. *J Plankton Res* 17:1587–1591
- Janowitz GS, Kamykowski D (1999) An expanded Eulerian model of phytoplankton environmental response. *Ecol Model* 118:237–247
- Kamykowski D, Yamazaki H (1997) A study of metabolism-influenced orientation in the diel vertical migration of marine dinoflagellates. *Limnol Oceanogr* 42:1189–1202
- Kamykowski D, Milligan EJ, Reed RE (1998) Biochemical relationships with the orientation of the autotrophic dinoflagellate, *Gymnodinium breve*, under nutrient-saturated conditions. *Mar Ecol Prog Ser* 167:105–117
- Lee ES, Lewitus AJ, Zimmer RK (1999) Chemoreception in a marine cryptophyte: behavioral plasticity in response to amino acids and nitrate. *Limnol Oceanogr* 44:171–174
- Liu G, Janowitz GS, Kamykowski D (2001) A biophysical model of population dynamics of the autotrophic dinoflagellate *Gymnodinium breve*. *Mar Ecol Prog Ser* 210: 101–124
- Marmorino GO (1983a) Summertime coastal currents in the northeastern Gulf of Mexico. *J Phys Oceanogr* 13:65–77
- Marmorino GO (1983b) Variability of current, temperature, and bottom pressure across the west Florida continental shelf, winter 1981–1982. *J Geophys Res* 88:4439–4457
- Maul GA (1975) Circulation of the eastern Gulf of Mexico and its possible relation to red tides. In: Joyce E (ed) Proceedings of Florida Red Tide Conference. Fla Mar Res Publ No. 8. p 9–10
- Mitchum GT, Sturges W (1982) Wind-induced currents on the West Florida Shelf. *J Phys Oceanogr* 12:1310–1317
- Odum HT, Lackey JB, Hynes J, Marshall N (1955) Some red tide characteristics during 1952–1954. *Bull Mar Sci Gulf Caribb* 5:247–258
- Penta B (2000) Phytoplankton competition on the West Florida Shelf: a simulation analysis with red tide implications. PhD dissertation. University of South Florida, St. Petersburg
- Rounsefell GA, Nelson WR (1966) Red tide research summarized to 1964 including an annotated bibliography. US Fish Wildl Serv Spec Sci Rep 535, Washington, DC
- Seliger HH, Carpenter JH, Loftus M, McElroy WD (1970) Mechanism for the accumulation of high concentrations of dinoflagellates in a bioluminescent bay. *Limnol Oceanogr* 15:234–245
- Seliger HH, Carpenter JN, Loftus ME, Biggley WH, McElroy WD (1971) Bioluminescence and phytoplankton successions in Bahia Fosforescente, Puerto Rico. *Limnol Oceanogr* 16:608–622
- Seliger HH, Tyler MA, Mckinley KR (1979) Phytoplankton distributions and red tides resulting from frontal circulation patterns. In: Taylor D, Seliger HH, Lewis C (eds) Toxic dinoflagellate blooms. Proc 2nd Int Conf, Elsevier, New York, p 239–248
- Shanley E, Vargo GA (1993) Cellular composition, growth, photosynthesis, and respiration rates of *Gymnodinium breve* under varying light levels. In: Smayda TJ, Shimizu Y (eds) Toxic phytoplankton blooms in the Sea. Elsevier, New York, p 831–836
- Steidinger KA (1973) Phytoplankton ecology: a conceptual review based on eastern Gulf of Mexico research. *CRC Crit Rev Microbiol* 3:49–67
- Steidinger KA (1975) Implications of dinoflagellate life cycles on initiation of *Gymnodinium breve* red tides. *Environ Lett* 9:129–139
- Steidinger KA, Baden DG (1984) Toxic marine dinoflagellates. In: Spector DL (ed) Dinoflagellates. Academic Press, Inc, New York
- Steidinger KA, Haddad K (1981) Biological and hydrographic aspects of red tides. *BioScience* 31:814–819
- Steidinger KA, Ingle RM (1972) Observations on the 1971 summer red tide in Tampa Bay, Florida. *Environ Lett* 3: 271–278
- Steidinger KA, Vargo GA (1988) Marine dinoflagellate blooms: dynamics and impacts. In: Lembi CA, Waaland JR (eds) Algae and human affairs. Cambridge University Press, New York, p 373–401
- Steidinger KA, Davis TJ, Williams J (1966) Observations of *Gymnodinium breve* Davis and other dinoflagellates. *Fla Board Conserv, Prof Pap Ser* 8:8–15
- Steidinger KA, Vargo GA, Tester PA, Tomas CR (1998) Bloom dynamics and physiology of *Gymnodinium breve* with emphasis on the Gulf of Mexico. In: Anderson DM, Cembella AD, Hallegraeff GM (eds) Physiological ecology of harmful algal blooms. Springer-Verlag, Berlin, p 133–153
- Tester PA, Steidinger KA (1997) *Gymnodinium breve* red tide blooms: Initiation, transport, and consequences of surface circulation. *Limnol Oceanogr* 42:1039–1051
- Tester PA, Stumpf RP, Vukovich FM, Fowler PK, Turner JT (1991) An expatriate red tide bloom: transport, distribution, and persistence. *Limnol Oceanogr* 36:1053–1061
- Tyler MA, Seliger HH (1978) Annual subsurface transport of a red tide dinoflagellate to its bloom area: water circulation patterns and organism distribution in the Chesapeake Bay. *Limnol Oceanogr* 23:227–246
- Vargo GA, Howard-Shamblott D (1990) Phosphorus requirements in *Ptychodiscus brevis*: cell phosphorus, uptake and growth requirement. In: Graneli E, Sundstrom B, Edler L, Anderson DM (eds) Toxic marine phytoplankton. Elsevier, Amsterdam, p 324–329
- Vargo GA, Shanley E (1985) Alkaline phosphatase activity in the red tide dinoflagellate *Ptychodiscus brevis*. *PSZN I: Mar Ecol* 6:251–264
- Willey JM, Waterbury JB (1989) Chemotaxis toward nitrogenous compounds by swimming strains of marine *Synechococcus* spp. *Appl Environ Microbiol* 55:1888–1894
- Wilson WB (1966) The suitability of sea-water for the survival and growth of *Gymnodinium breve* Davis, and some effects of phosphorous and nitrogen on its growth. *Fla Board Conserv Mar Res Lab* 7:1–42